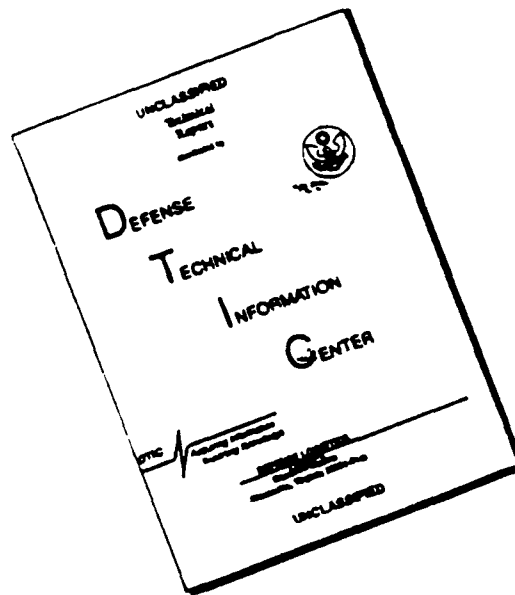


1. AGENCY USE ONLY (Leave blank)		2. REPORT DATE 31 Dec 93		3. REPORT TYPE AND DATES COVERED Final 1 Oct 91 - 30 Sep 93	
4. TITLE AND SUBTITLE Scalar Imaging Velocimetry Studies of Turbulent Flow Structure and Dynamics (U)				5. FUNDING NUMBERS PE - 61102F PR - <del>2308</del> 2307 / BS SA - BS G - F49620-92-J-0025	
6. AUTHOR(S) Werner J.A. Dahm				7. PERFORMING ORGANIZATION REPORT NUMBER AFOSR-TR- 94 0164	
7. PERFORMING ORGANIZATION(S) AND ADDRESS(ES) Gas Dynamics Laboratories Department of Aerospace Engineering The University of Michigan Ann Arbor, MI 48109-2118				8. PERFORMING ORGANIZATION REPORT NUMBER F49620- 92-J-0025	
9. SPONSORING ORGANIZATION NAME(S) AND ADDRESS(ES) AFOSR/NA 110 Duncan Avenue, Suite B115 Bolling AFB, DC 20332-0001				10. SPONSORING ORGANIZATION REPORT NUMBER NA	
11. SUPPLEMENTARY NOTES					
12a. DISTRIBUTION / AVAILABILITY STATEMENT Approved for Public Release; distribution is unlimited				12b. DISTRIBUTION CODE	
13. ABSTRACT (Maximum: 200 words)  The first fully-resolved, non-intrusive, experimental measurements of the spatio-temporal structure and dynamics of the full nine-component velocity gradient tensor field $\nabla u(x,t)$ in a turbulent flow are here obtained by applying the scalar imaging velocimetry technique [Phys. Fluids A 4, 2191-2206] to laboratory turbulent flow scalar field data. A variational method implementing this concept is described in which weighted residuals of the conserved scalar transport equation, the continuity condition, and a derivative smoothness condition are minimized over the space of velocity fields. The technique is applied to direct numerical simulation (DNS) data for the limiting case of turbulent mixing of a $Sc = 1$ passive scalar field. The spatial velocity fields $u(x,t)$ obtained correlate well with the exact DNS results, as do statistics of the velocity and velocity gradient fields. The method is then applied to fully resolved four-dimensional $Sc \gg 1$ scalar field imaging measurements from a laboratory turbulent flow. Results give the first fully resolved data for the time-varying $(u, v, w)$ vector velocity component fields simultaneously everywhere on a regular three-dimensional spatial grid in a turbulent flow. Direct differentiation of these fields yields the spatial structure in the full velocity gradient tensor field components. From these, the vector vorticity field $\omega(x,t)$ and tensor strain rate field $\epsilon_{ij}(x,t)$ are extracted, as are the kinetic energy density field $k(x,t)$ , the kinetic energy dissipation rate field $\Phi(x,t)$ , and the enstrophy field $W(x,t)$ . Finally, extraction of the time evolution in these fields is demonstrated by applying this scalar imaging velocimetry method to perform the inversion for the velocity field at several sequential time steps.  DISSEM BY REQUESTED 3					
14. SUBJECT TERMS Turbulent flows; Flow diagnostics; Turbulence structure and dynamics				15. NUMBER OF PAGES 74	
17. SECURITY CLASSIFICATION OF THIS REPORT Unclassified				18. PRICE CODE	
17. SECURITY CLASSIFICATION OF THIS PAGE Unclassified		19. SECURITY CLASSIFICATION OF ABSTRACT Unclassified		20. LIMITATION OF ABSTRACT UL	

94 4 20 081

# DISCLAIMER NOTICE



THIS DOCUMENT IS BEST  
QUALITY AVAILABLE. THE COPY  
FURNISHED TO DTIC CONTAINED  
A SIGNIFICANT NUMBER OF  
PAGES WHICH DO NOT  
REPRODUCE LEGIBLY.

AFOSR-TR- 94 0164

Approved for public release;  
distribution unlimited.

### Executive Abstract

The first fully-resolved, non-intrusive, experimental measurements of the spatio-temporal structure and dynamics of the full nine-component velocity gradient tensor field  $\nabla \mathbf{u}(\mathbf{x}, t)$  in a turbulent flow have been obtained by applying the scalar imaging velocimetry technique [*Phys. Fluids A* 4, 2191-2206] to turbulent flow scalar field data. A variational method for implementing this technique is described, in which weighted residuals of the conserved scalar transport equation, the continuity condition, and a derivative smoothness condition are minimized over the space of velocity fields. The technique is applied to direct numerical simulation (DNS) data for the limiting case of turbulent mixing of a  $Sc = 1$  passive scalar field. The spatial velocity fields  $\mathbf{u}(\mathbf{x}; t)$  obtained correlate well with the exact DNS results, as do statistics of the velocity and velocity gradient fields. The method is then applied to fully resolved four-dimensional  $Sc \gg 1$  scalar field imaging measurements from a laboratory turbulent flow. Results give the first fully-resolved data for the time-varying  $(u, v, w)$  vector velocity component fields simultaneously everywhere on a regular three-dimensional spatial grid. Direct differentiation of these fields yields the spatial structure in the full velocity gradient tensor field components. From these, the vector vorticity field  $\omega_i(\mathbf{x}, t)$  and tensor strain rate field  $\epsilon_{ij}(\mathbf{x}, t)$  are extracted, as are the kinetic energy density field  $k(\mathbf{x}; t)$ , the kinetic energy dissipation rate field  $\Phi(\mathbf{x}; t)$ , and the enstrophy field  $W(\mathbf{x}; t)$ . Finally, extraction of the time evolution in these fields is demonstrated by applying this scalar imaging velocimetry method to perform the inversion for the velocity field at several sequential time steps.

94-12064



Accession For	
NTIS GRA&I	<input checked="checked" type="checkbox"/>
DTIC TAB	<input type="checkbox"/>
Unannounced	<input type="checkbox"/>
Justification	
By	
Distribution/	
Availability Codes	
Dist	Avail and/or Special
A-1	

## 1. Introduction and Overview

This research program at Michigan represents a combined experimental and theoretical effort with the following three major objectives:

- (i) to *develop* a new, quantitative, high-resolution, four-dimensional, spatio-temporal, scalar imaging diagnostic technique capable of yielding direct experimental measurements of the structure and dynamics of the vector velocity, vorticity, and tensor strain rate fields at the dissipative scales of real laboratory turbulent flows,
- (ii) to *use* this new measurement capability to experimentally determine the detailed physical characteristics associated with the spatial structure and temporal dynamics of the dissipative scales of motion in high Reynolds number turbulent flows, and
- (iii) to *incorporate* results from these novel measurements into an improved understanding for the spatio-temporal characteristics of the fine scales of turbulence, in order to contribute to the development of new models for the small scales that will permit practical engineering computations of turbulent flows.

Information on the fully-resolved, three-dimensional, spatial structure and simultaneous temporal dynamics of the full nine-component velocity gradient tensor field  $\nabla \mathbf{u}(\mathbf{x}, t)$  at the small scales of turbulent flows is key to the development of physically-based models for these scales of turbulence. These scales are generally presumed to be quasi-universal in high Reynolds number flows, and thus studied in a generic context. To date, this has been done almost exclusively via direct numerical simulations (DNS) of the Navier-Stokes equations. More recently, there have been dramatic advances in experimental techniques for whole field measurements in turbulent flows, which are beginning to allow direct experimental studies of the structure and dynamics of velocity and scalar fields in turbulence at a level of resolution and detail entirely comparable to DNS and at parameter values inaccessible to such numerical simulations. These techniques are demonstrating a potential that would have been unthinkable as recently as five years ago. They are proving to be the next stage in a revolution that is providing detailed access to turbulence structure and dynamics, permitting studies of real, spatially-developing turbulent flows in nonperiodic domains, at conditions beyond the reach of DNS.

Our work under this AFOSR grant has been aimed at studies of the dissipative scales of turbulence. We use a molecular tracer together with high-speed, high-resolution

imaging methods to allow access to the finest scales of motion in the flow. These allow fully-resolved, four-dimensional, spatio-temporal measurements of a dynamically passive, conserved scalar quantity  $\zeta(\mathbf{x},t)$  being mixed by the flow. The work under this AFOSR grant has been based on a new technique we have developed [*Phys. Fluids A* 4, 2191-2206] that allows these conserved scalar field measurements to be used to extract the underlying vector velocity field  $\mathbf{u}(\mathbf{x},t)$ , along with the vector vorticity and tensor strain rate fields, at the dissipative scales of turbulent flows. This has produced the first fully-resolved, non-intrusive, experimental measurements of the spatio-temporal structure and dynamics of the full nine-component velocity gradient tensor field  $\nabla\mathbf{u}(\mathbf{x},t)$  in a turbulent flow. These wholly new data are now being used to develop physically-based models for the small scales in large eddy simulations of turbulent flows.

## 1.1 Background

Experiments capable of directly yielding useful information on the detailed structure and dynamics of velocity gradients in turbulence have been few. Most have been limited to single-point measurements of a small subset of the full velocity gradient tensor field. The earliest and still the most widely used of these experimental techniques allow measurement of one or more of the gradient tensor components rely on multiple hot-wire or hot-film probes. The original four hot-wire probe was developed in 1950 by Kovasznay (1954) for measurements of the streamwise component  $\omega_1$  of the vorticity vector at a single spatial point. Corrsin & Kistler (1954), and later Willmarth & Lu (1972), Willmarth & Bogar (1977), and Kastrinakis *et al* (1977, 1979, 1983) used probes of this type for streamwise vorticity component measurements in turbulent boundary layers. Vukoslavcevic & Wallace (1981) subsequently developed an improved Kovasznay-type probe for the streamwise vorticity that had four independent wires to overcome parasitic effects between the various sensors. Foss (1981), Foss *et al* (1986, 1987), and Haw, Foss & Foss (1989) have successfully used a similar four hot-wire arrangement to measure the cross-stream component  $\omega_3$  of the vorticity vector at a single point. A five-sensor hot-film probe for simultaneously measuring the spanwise and normal vorticity components,  $\omega_2$  and  $\omega_3$ , was developed and used by Eckelmann *et al* (1977) and Wallace, Brodkey & Eckelmann (1977). Surveys of some of the characteristics of these vorticity probes and the data obtained from them are given by Wallace (1986) and by Foss & Wallace (1989). Kim & Fiedler (1989) subsequently used a six-sensor probe for simultaneous measurement of the streamwise and cross-stream vorticity components,  $\omega_1$  and  $\omega_3$ . More recently, Vukoslavcevic, Wallace & Balint (1991), Balint, Vukoslavcevic & Wallace (1991) have succeeded in building and using a nine-sensor hot-wire probe that yields simultaneous measurements for all three vorticity components  $\omega_1$ ,

$\omega_2$ , and  $\omega_3$ . This probe permits resolution of the vorticity vector at a scale approximately six times coarser than the local Kolmogorov scale at their measurement location in a thickened turbulent boundary layer. Kit *et al* (1987, 1988) have developed a nine-wire probe to measure components of the velocity gradient tensor, and even more recently Tsinober, Kit & Dracos (1992) have assembled a 12-sensor hot-wire probe, and even a 20-sensor probe, without any common prongs, for measuring all nine independent components of the velocity gradient tensor at a single spatial point. In their grid turbulence experiment, this probe allowed resolution of lengthscales roughly five times coarser than the local Kolmogorov scale.

Despite the successes in development of these multiple hot-wire/film probes, all have certain characteristics in common that ultimately influence their ability to provide data on the structure and dynamics in the velocity gradient tensor field. Firstly, even in principle they allow time series measurements at only a single spatial "point," with one-dimensional spatial structure in the velocity gradient component fields discernible only if a Taylor hypothesis is accepted. Of a more practical nature, interference between the various wires and prongs in such probes leads, at a minimum, to complex calibrations and the potential for erroneous measurements [e.g. see Vukoslavcevic, Wallace & Balint (1991), Tsinober, Kit & Dracos (1992)]. Moreover, as the number of sensor wires and prongs in these invasive probes increases to measure more components of the local velocity gradient tensor, the probe size increases and blockage effects can become significant, altering the velocity gradients within the wire farm at the probe tip.

In part to overcome these concerns about intrusive probes, non-invasive optical techniques have been increasingly used in recent years to measure certain velocity gradient components. Lang (1985) developed an LDV with four focal volumes to measure the spanwise vorticity in a turbulent shear layer. More recent advances in laser diagnostics and high-speed data acquisition and processing capabilities have facilitated a variety of optically-based, non-intrusive velocimetry techniques which provide information over spatial fields of many points. Reviews of some of these are given, for example, by Adrian (1986, 1991), Lauterborn & Vogel (1984), and Gad-el-Hak (1989). Being optically-based, these techniques potentially offer high spatial and temporal resolution, as well as genuine field information rather than single-point data. The most widely used are particle image velocimetry techniques. These generally produce two-component velocity vectors over two-dimensional fields, though three-dimensional particle tracking [4, 5] and holographic particle image velocimetry [6, 7] are being developed for measuring full, three-component vector velocity fields in complex flows. However, as with all particle imaging techniques, the seeding densities required to adequately resolve the finest veloci-

ty gradient lengthscales in turbulent flows makes optical penetration into the flow difficult, and potentially limits these methods for studies of the fine structure and dynamics of velocity gradient fields in turbulent flows. This optical penetration difficulty can be circumvented by using an effectively continuous distribution of laser fluorescent dye molecules as the seed, whose size eliminates the Mie scattering associated with particulates and thus maintains optical transparency in the flow field. Determining velocities then no longer centers on finding discrete particle displacements, but rather on inversion of the time-evolving dye concentration field to extract the underlying velocity field. Often the dye molecules are both dynamically passive and conserved, so that the conserved scalar transport equation governs their concentration field evolution and extraction of the velocity field can begin from this equation. Such scalar-based velocimetry techniques were first introduced in Ref. 1.

Here we demonstrate the first application of the scalar imaging velocimetry concept to laboratory measurements of a conserved scalar field in a turbulent flow, and extract the underlying velocity gradient tensor field as well as its time evolution. As before, we approach the problem of determining the fully resolved, space- and time-varying velocity field  $\mathbf{u}(\mathbf{x}, t)$  from the standpoint of the exact conserved scalar transport equation. A variational method for implementing this concept is described in Sec. II, in which weighted residuals of the conserved scalar transport equation, the continuity condition, and a derivative smoothness condition are minimized over the space of velocity fields. The technique is then applied in Sec. III to direct numerical simulation data for the limiting case of turbulent mixing of a  $Sc = 1$  passive scalar field. The spatial velocity fields  $\mathbf{u}(\mathbf{x}; t)$  obtained are compared with the exact DNS results to assess the validity of the method. In Sec. IV, the method is then applied to fully resolved four-dimensional  $Sc \gg 1$  scalar field imaging measurements from a laboratory turbulent flow. We extract the time-varying full vector velocity component fields simultaneously everywhere on a regular three-dimensional spatial grid. Direct differentiation of these fields yields the spatial structure in the full velocity gradient tensor field components  $\nabla \mathbf{u}(\mathbf{x}; t)$ . From these, the vector vorticity and tensor strain rate fields are given, as are the kinetic energy density field the kinetic energy dissipation rate field, and the enstrophy field. Extraction of the time evolution in these fields is also demonstrated by applying this scalar imaging velocimetry method to perform the inversion for the velocity field at several sequential time steps. In Sec. V we conclude with a discussion of the suitability of this technique for large scale studies of the structure and dynamics of the small scales of turbulent flows, and comment of the possible extension to lower  $Sc$  scalar field measurements, offering access to the velocity gradient fields over a wider range of lengthscales.

## 2. The Scalar Imaging Velocimetry Technique

In this section, we describe the scalar imaging velocimetry method implemented here to determine the vector velocity field  $\mathbf{u}(\mathbf{x}, t)$  from fully resolved, four-dimensional measurements of a single, dynamically passive, conserved scalar field  $\zeta(\mathbf{x}, t)$  in turbulent flows. This implementation expands on that in Ref. 1 in its use of variational techniques in the velocity field extraction. The underlying conserved scalar field measurement technique will be reviewed here only briefly; details can be found in Refs. 7-9.

### A. Scalar field measurements

Any dynamically passive conserved scalar field  $\zeta(\mathbf{x}, t)$  evolves via the advection-diffusion equation

$$\frac{\partial \zeta}{\partial t} + \mathbf{u} \cdot \nabla \zeta - \frac{1}{ReSc} \nabla^2 \zeta = 0 \quad , \quad (1)$$

where all quantities are normalized by reference length and velocity scales  $l^*$  and  $u^*$ . The dimensionless scalar diffusivity  $1/ReSc$  (the Peclet number) involves the Reynolds number  $Re = (u^* l^* / \nu)$  and Schmidt number  $(\nu/D)$ , with  $\nu$  and  $D$  being respectively the vorticity and scalar diffusivities. Scalar imaging velocimetry involves inversion of (1), together with additional conditions, based on measurements of the scalar field. The requisite measurements must therefore be fully-resolved in both space and time, while at the same time having sufficient signal quality, to allow direct differentiation of the scalar field data to evaluate the derivatives appearing in (1).

Such fully-resolved four-dimensional scalar field measurements are based on successive, high-speed, planar imaging of the laser induced fluorescence from a dynamically passive laser dye carried by the flow, whose concentration is a conserved scalar variable. A collimated laser beam is repeatedly swept in a raster fashion throughout a small volume in the flow by a pair of low-inertia mirrors driven by two galvanometric scanners slaved to the imaging array timing. The successive  $256 \times 256$  scalar field data planes are acquired at rates up to 142 planes/sec into gigabyte sized data sets using very fast computer disk ranks to produce a four-dimensional spatio-temporal data space structured as shown in Fig. 1. Each such measured data space consists of a rapid succession of individual three-dimensional spatial data volumes for  $\zeta(\mathbf{x}; t)$ . Each of these data volumes in turn consists of a sequence of two-dimensional spatial data planes, each consisting of an array of  $256 \times 256$  individual data points. There are over three billion data points comprising the scalar field data space resulting from each such measurement. The flow facility and imaging electronics are designed so that the resulting effective spatial resolution ( $\Delta x$ ,  $\Delta y$ ,



$\Delta z$ ) between adjacent points in each three-dimensional data volume is smaller than the local strain-limited molecular diffusion scale  $\lambda_D \delta \sim Sc^{-1/2} Re_\delta^{-3/4}$  of the scalar field. Similarly, the temporal resolution  $\Delta t$  between the same data point in successive spatial data volumes can be held smaller than the local molecular diffusion scale advection time  $\lambda_D / u$ . This resolution, together with the high signal quality attained, allows accurate differentiation of the measured conserved scalar field data in all three space dimensions and in time to determine the components of the instantaneous time derivative field  $(\partial/\partial t)\zeta(\mathbf{x}, t)$ , the scalar gradient vector field  $\nabla\zeta(\mathbf{x}, t)$ , and even  $\nabla^2\zeta(\mathbf{x}, t)$  throughout the four-dimensional data space. Such fully-resolved conserved scalar field measurements have been conducted at outer-scale Reynolds numbers  $Re_\delta \equiv (u\delta/\nu)$  as high as 6,000. An example of a single three-dimensional spatial data volume obtained via this technique is shown in Fig. 2.

Note that, for dilute solutions in water, the scalar diffusivity of the dye is quite small, with  $Sc \approx 2075$ . As a consequence, the underlying velocity field which we are aiming here to extract from such measurements is considerably smoother than the scalar field from which we begin. In particular, the finest gradient lengthscale in  $\lambda_v$  in the velocity field is larger, by a factor of  $Sc^{1/2}$ , than the smallest gradient lengthscale  $\lambda_D$  in the scalar field. For the  $Sc$  in the laboratory data in Section IV, this ratio of scales is about 45. However, for the  $Sc = 1$  DNS data in Section III, this ratio is only 1 and thus extraction of the velocity field is more difficult.

#### B. Formulation of the variational problem

The relation between the scalar field and the underlying velocity field comes solely through  $\mathbf{u} \cdot \nabla\zeta$  in (1). Previously<sup>1-3</sup>, we have inverted this equation directly to obtain the local projection  $u_{||}(\mathbf{x}, t)$  of the velocity vector onto the scalar gradient unit vector, namely

$$u_{||}(\mathbf{x}, t) \equiv \mathbf{u}(\mathbf{x}, t) \cdot \frac{\nabla\zeta(\mathbf{x}, t)}{|\nabla\zeta(\mathbf{x}, t)|} \quad (2)$$

The full vector velocity field  $\mathbf{u}(\mathbf{x}, t)$  was then uniquely determined from the  $\nabla u_{||}(\mathbf{x}, t)$  field via an iterative scheme incorporating a smoothness assumption that becomes increasingly valid as  $Sc$  increases. The zeroth iteration estimate  $\mathbf{u}^0(\mathbf{x}, t)$  was found by direct inversion, at each point in the domain, of the local  $3 \times 3$  linear system formed by writing (2) for triplets of closely spaced points having sufficiently noncolinear scalar gradients. Subsequent iterations incorporated the velocity gradients  $\nabla \mathbf{u}^{n-1}(\mathbf{x}, t)$  obtained from the previous iteration in the calculation of the  $n$ -th estimate  $\mathbf{u}^n(\mathbf{x}, t)$ . Convergence was stable and rapid, with the final result for  $\mathbf{u}(\mathbf{x}, t)$  typically achieved for  $Sc \gg 1$  after just two or three iterations. This direct-inversion implementation was shown to produce accurate re-

sults for a wide range of test cases – for details see Ref. 1.

Despite the high resolution and signal quality of the underlying scalar field measurements from Ref. 11, small but unavoidable errors will be introduced in the various scalar field derivatives in (1) and (2). As a consequence, even if the *true*  $u(x,t)$  were introduced in (1), then as a direct result of these small errors in the  $\zeta(x,t)$  derivative fields, the right hand side would in fact *not* quite be zero. In effect, strict enforcement of the zero right side in (1) introduces errors in the velocity field obtained from this direct-inversion approach. These considerations in turn naturally motivate a *variational* approach to the inversion problem, in which the right side in (1) is not forced to zero, but rather is minimized over the space of possible velocity fields, subject to a smoothness constraint as before. In effect, we do not seek the velocity field that produces the clearly spurious zero right side in (1), but instead take the velocity field  $u(x,t)$  that minimizes the integral of the right side over the entire domain as an optimal representation of the true velocity field. Formally, we minimize the integral of a function  $E$  over the domain  $D$  as

$$\int_D E(u_1, u_2, u_3; x_1, x_2, x_3) d^3x = \min, \quad (3)$$

where  $E$  is composed of residuals representing deviations from conserved quantities, including (1), as well as conditions measuring the smoothness in the  $u(x,t)$  solution.

### C. Specification of the variational equations

As noted above, the integral minimization in (3) aims to find the *one* velocity field that best satisfies the scalar transport equation in (1) while at the same time satisfying an appropriate smoothness condition. In general, the function  $E$  can be written as a sum of an arbitrary number of such conditions

$$E \equiv E_1 + \alpha^2 E_2 + \beta^2 E_3 + \dots, \quad (4)$$

where each of the  $E_i \geq 0$  represent a local condition involving the velocity field and, possibly, the scalar field. The adjustable factors ( $\alpha^2, \beta^2, \dots > 0$ ) allow control over the relative weights assigned to these individual conditions in the minimization function  $E$ . In our case, the term  $E_1$  is chosen as the right side in (1), namely the condition that the (known) scalar field derivatives and any candidate velocity field be in “good” agreement with the scalar transport equation (1). Thus formally

$$E_1 \equiv \left\{ \left[ \frac{\partial}{\partial t} + \mathbf{u} \cdot \nabla - \frac{1}{ReSc} \nabla^2 \right] \zeta(x,t) \right\}^2. \quad (5)$$

The smoothness condition, as well as any additional conditions, must be specified in a manner consistent with the numerical scheme by which the minimum in (4) is to be

found. In particular, writing (4) for a set of  $N$  discrete points in the domain  $D$  leads to a system of  $3N$  simultaneous equations for the velocity components  $u_i$  for  $i = \{1, 2, 3\}$  at each of the  $N$  points. In general this system will be very large. Consequently, we confine our interest to conditions that will produce a *linear* system, so that the simplicity afforded by linear inversion methods can be employed in the solution for  $\mathbf{u}(\mathbf{x}, t)$ . This, in turn, demands that the derivatives  $(\partial E_j / \partial u_i)$  should be linear in the components  $u_i$ , and thus that the conditions be at most second-order in  $\mathbf{u}$ . Among this restricted set of conditions, one is immediately obvious, namely the incompressibility condition  $\nabla \cdot \mathbf{u} = 0$ . This is represented in non-negative form as

$$E_2 \equiv \{\nabla \cdot \mathbf{u}\}^2. \quad (6)$$

However while inclusion of this incompressibility condition is certainly desirable, it firstly does not impart the requisite smoothness on the solution, and secondly suffices to determine the solution in two dimensional flows only. An explicit smoothness condition that satisfies these conditions is necessary. Ideally, this would be a direct mathematical representation of a specific physical property of the flow. Unfortunately, the existence of flow properties which can be represented as minimizations of integral quantities is very limited – e.g. to certain simple inviscid, circulation-preserving flows; see Truesdell<sup>12</sup>. Here we choose to minimize the velocity gradients by the condition

$$E_3 \equiv \{\nabla \mathbf{u} : \nabla \mathbf{u}\}. \quad (7)$$

The physical implications of this condition can be understood from the kinetic energy transport equation, where (7) includes both the work done by the viscous stresses and the kinetic energy dissipation by the viscous stresses. Incorporating (7) as the smoothness condition thus acts to imitate the fluid viscosity as it smoothes out strong gradients and pursues a condition of minimized kinetic energy dissipation.

Note that explicit agreement with these conditions is not being enforced; rather, we require only that the deviations from these conditions be minimized in the weighted sense prescribed in (3) and (4). Since the integral in (3) involves the three dependent variables  $u_i$  and three independent variables  $x_i$ , standard variational calculus lead to the three variational (Euler) equations

$$u \zeta_x^2 + v \zeta_x \zeta_y + w \zeta_x \zeta_z - (\alpha^2 + \beta^2)(u_{xx} + v_{yy} + w_{zz}) - \beta^2 \nabla^2 u = -\left(\frac{\partial \zeta}{\partial t} - \frac{1}{ReSc} \nabla^2 \zeta\right) \zeta_x, \quad (9)$$

$$u \zeta_x \zeta_y + v \zeta_y^2 + w \zeta_y \zeta_z - (\alpha^2 + \beta^2)(u_{xy} + v_{yy} + w_{yz}) - \beta^2 \nabla^2 v = -\left(\frac{\partial \zeta}{\partial t} - \frac{1}{ReSc} \nabla^2 \zeta\right) \zeta_y, \quad (10)$$

$$u \zeta_x \zeta_z + v \zeta_y \zeta_z + w \zeta_z^2 - (\alpha^2 + \beta^2)(u_{xz} + v_{yz} + w_{zz}) - \beta^2 \nabla^2 w = -\left(\frac{\partial \zeta}{\partial t} - \frac{1}{ReSc} \nabla^2 \zeta\right) \zeta_z, \quad (11)$$

where subscripts denote spatial derivatives. The solution of these equations gives the velocity field  $\mathbf{u}(\mathbf{x};t)$  that minimizes (3) - (7) for the given scalar field data  $\zeta(\mathbf{x},t)$ . Note that these equations are linear in the velocity components ( $u, v, w$ ).

Finding the solution for the velocity field involves discretizing (9) - (11) and writing these three equations for each of the points in each three-dimensional spatial data volume. In doing this we order the  $N$  points in each volume by indexing successively in  $x$ ,  $y$ , and  $z$ . We then construct three  $N$ -dimensional vectors containing the velocity components  $u$ ,  $v$ , and  $w$  at each of these points, and finally concatenate these to form a single  $3N$ -dimensional vector representing the velocity field  $\mathbf{u}(\mathbf{x};t)$ . The above equations can then be written as a linear system of the form

$$\mathbf{A}\mathbf{u} = \mathbf{b} \quad (12)$$

where  $\mathbf{A}$  is a  $3N \times 3N$  matrix containing the (known) scalar field derivatives appearing on the left in (9) - (11), and  $\mathbf{b}$  is a  $3N$ -dimensional vector containing the (known) scalar field derivatives on the right side in these equations. Solving (12) for the (unknown) velocity field  $\mathbf{u}$  simply requires inverting the matrix  $\mathbf{A}$ . However, owing to the size of this matrix in the cases for which results are presented here, direct solution methods are impractical. We therefore use standard linear iterative methods, in this case Gauss-Seidel and SOR iteration. Classical stability requirements for convergence of such iterative methods place restrictions on the range of  $\alpha$  and  $\beta$  in (4). We use  $\alpha \approx 0.10$  and  $\beta = 0.15$  in the results presented here. The iteration is begun with  $\mathbf{u} \equiv 0$  as the initial estimate.

Note that minimization of  $E_2$  and  $E_3$  in (6) and (7) can occur by reduction of the average velocity magnitude over the entire domain, as well as by reduction of the resulting scaled velocity gradients. The  $\mathbf{u}$  in these conditions thus "floats." Inclusion of  $E_2$  and  $E_3$  in (4) will therefore reduce the average velocity magnitude by an amount that depends on  $\alpha$  and  $\beta$ . It is only through  $E_1$  that the average velocity magnitude tied to an absolute level set by the scalar field derivatives. The velocity field  $\mathbf{u}$  that results from (12) is therefore finally reinserted in (3) to determine the uniform multiplicative constant that minimizes  $E_1$  over the entire domain.

#### *D. Features of the variational formulation*

Aside from the key differences noted above, it is insightful to compare certain other aspects of the variational scalar imaging velocimetry formulation given in (9) - (12) with the direct-inversion formulation in Ref. 1. In the latter, determination of the velocity vector at a given point  $\mathbf{x}$  in the data volume relies on scalar field information from points within a small neighborhood of  $\mathbf{x}$ . This results from writing (2) for triplets of points to solve for the three unknowns  $u$ ,  $v$ , and  $w$  under the assumption that, for the zeroth itera-

tion estimate, the velocity  $u$  at each of these three points is the same. Furthermore, multiple triplets are formed at each point to allow reduction of noise effects. This smoothness condition in the direct-inversion approach is easily justified for  $Sc \gg 1$  scalar field data, since the scalar field then varies on much finer scales than does the velocity field. In effect, the velocity field sought has a far lower level of detail than does the scalar field data from which the calculation proceeds. However, at  $Sc \approx 1$ , the comparable characteristic length scales in the velocity and scalar fields affords no redundancy of scalar field information for the determination of the velocity field. In that case, the scalar and velocity fields both possess roughly the same amount of detail. In the context of inversion-based scalar imaging velocimetry, this renders the imposition of smoothness and noise reduction for  $Sc \approx 1$  difficult; at the same time, this points out two particularly attractive features of the variational formulation, namely its strictly local nature and its comparative insensitivity to noise in the scalar field data.

The insensitivity to noise in the scalar field measurements is implicit in the use of residuals (5-7) in the variational formulation. The significance of the local nature of the scheme can be understood as follows. Note that in the variational formulation, the determination of the velocity vector at any given point involves information at that point and its immediate neighbors only, specifically those neighbors sufficient to calculate spatial derivatives. No assumptions are made about the relative level of detail in the velocity and scalar fields. The local nature of the variational formulation thus makes it fully applicable to any turbulent flow scalar field data for which the spatial resolution is sufficient to resolve the smallest expected velocity field lengthscales. In particular, the variational scalar imaging velocimetry scheme can be applied to fully resolved scalar field information in turbulent flows at Schmidt numbers of one and higher.

### 3. A DNS Test for $Sc = 1$

In this section, the variational scalar imaging velocimetry method described above is applied to scalar field data obtained from a direct numerical simulation (DNS) of  $Sc = 1$  passive scalar mixing in a turbulent flow. The use of DNS data, as opposed to synthetically generated test fields, provides the detailed velocity field against which, as a test of the variational scalar imaging velocimetry scheme at low Schmidt number, we will make use of a direct numerical simulation of a turbulent flow at  $Sc = 1$ . The velocity fields obtained through application of the scalar imaging velocimetry technique can be compared with the actual velocity fields used in the simulation, allowing us to quantify the accuracy of the technique.

We use the DNS data of Mell, Kosály & Riley (1992) for turbulent mixing of a dynamically passive  $Sc = 1$  conserved scalar quantity in a decaying, homogeneous, isotropic, incompressible, turbulent flow. The Taylor scale Reynolds number  $Re_\lambda$  decays from its initial value of 92 to 65 at the time chosen for this test. A sample scalar field plane from this simulation at this time is shown in Fig. 3a. The computations were performed on a  $128^3$  volume. Scalar field derivatives were computed in  $128 \times 128 \times 13$  point sub-volumes, which were then subsampled to  $64 \times 64 \times 7$  point domains for this test. With  $\Delta x = \Delta y = \Delta z$ , the limited span in the third (z-) dimension was chosen to be characteristic of available fully resolved experimental scalar field data. The grid resolution was  $\Delta x = 0.1 \lambda_T$ , and the time separation between successive volumes used in this test was  $\Delta t = 0.07 \lambda_T / u_{rms}$ , again to mimic the characteristics of currently available fully resolved experimental scalar field data.

The scalar field derivatives  $\partial\zeta/\partial t$ ,  $\nabla\zeta$ , and  $\nabla^2\zeta$  are the only inputs to the variational formulation in (9) - (12). These are obtained via linear central differences from the scalar field data, and are shown in Figs. 3b-d for the same scalar field plane. The velocity field is then obtained by inverting (12) for the given scalar derivative matrix **A** and vector **b**. For the volume dimensions used here, the vector **b** contains 86,016 elements, and the matrix **A** consists of  $7.4 (10^9)$  elements, of which  $1.7 (10^6)$  are non-zero. The Gauss-Seidel iteration on this system, using a non-optimized code, typically required about an hour on an HP9000/735 workstation. The resulting individual velocity vector component fields are shown in Fig. 4. Shown also in this figure are the actual DNS velocity vector component fields for comparison. It is evident by examining these that the variational scalar imaging velocimetry method yields results for velocity vector field which are in good agreement with the exact values. To quantify this agreement, we use

of the conventional fluctuation correlation

$$R_{AB} \equiv \frac{\overline{u'_A u'_B}}{(\overline{u'^2_A})_{rms} (\overline{u'^2_B})_{rms}} \quad (13)$$

where the primes denote fluctuations, and the subscripts *A* and *B* refer to the SIV and DNS fields. The correlations obtained for the *u*, *v*, and *w* fields are given in Table 1, where 1.00 represents perfect correlation. That the *w* component has the poorest correlation is not surprising, given that the data volume has only one-tenth the extent in the *z*-direction that it has in the *x*- and *y*-directions. Thus the one-sided velocity derivatives required at the limits of the volume are more likely to affect the accuracy of the *z*-direction velocity component than the others. Nevertheless, the correlation levels obtained are quite high. The departures from perfect correlation would appear to result primarily from the smoothness condition  $E_3$  in (7), since the other two conditions in (3) should be identically zero.

Component	$R_{AB}$
<i>u</i>	0.94
<i>v</i>	0.94
<i>w</i>	0.91

Table 1. Correlations between the velocity vector component fields resulting from the scalar imaging velocimetry method and the exact DNS results for the  $Sc \approx 1$  case.

As a further demonstration of the agreement between the DNS fields and the scalar imaging velocimetry results, Fig. 5 presents distributions of the values of the velocity components *u*, *v*, and *w* for both the DNS and SIV fields. To emphasize that the important comparison is of the forms of these distributions, the velocity component values for each field have been normalized by their second moments. The similarity in the resulting distributions is evident in this figure.

It must also be noted that this  $Sc = 1$  test case is extremely demanding for any scalar-based velocimetry technique, since the scalar and velocity fields in this case each contain the same spatial length scales. The velocity field being sought therefore has the same information content as does the scalar field on which its extraction is based. Thus there is no redundancy of scalar field information. By comparison, at  $Sc \gg 1$  the information content in the scalar field far exceeds that in the velocity field, and this redundancy should make extraction of the underlying velocity field even more accurate.

The primary interest in this scalar imaging velocimetry technique is the access it offers to spatial structure and temporal dynamics of the full nine-component velocity gradient tensor. Accordingly Fig. 6 compares three typical components of  $\nabla \mathbf{u}(\mathbf{x}, t)$  with their DNS counterparts. Note that the structure and magnitudes of these tensor components is very similar in both cases. Indeed the visual comparison appears better than that in Fig. 4, however the quantitative correlations are actually lower. The complete tensor correlation  $R_{AB}$ , defined as

$$R_{AB} \equiv \frac{\overline{\left( \frac{\partial u_i}{\partial x_j} \right)_A \left( \frac{\partial u_i}{\partial x_j} \right)_B}}{\left\{ \overline{\left( \frac{\partial u_i}{\partial x_j} \right)_A^2} \right\}^{1/2} \left\{ \overline{\left( \frac{\partial u_i}{\partial x_j} \right)_B^2} \right\}^{1/2}} \quad (14)$$

is 0.783. Table 2 gives the individual tensor component correlations in (13) obtained for all nine gradient tensor component fields. Note that for the  $\partial u/\partial y$ ,  $\partial v/\partial z$ , and  $\partial w/\partial x$  component fields in Fig. 5 the correlations are 0.79, 0.83 and 0.75 respectively. The surprisingly better visual comparisons than in Fig. 4, for which the correlations are in fact significantly higher, apparently result from the larger number of features available as landmarks for comparison in the gradient fields.

Component	$R_{AB}$
$\partial u/\partial x$	0.80
$\partial u/\partial y$	0.79
$\partial u/\partial z$	0.80
$\partial v/\partial x$	0.80
$\partial v/\partial y$	0.80
$\partial v/\partial z$	0.83
$\partial w/\partial x$	0.75
$\partial w/\partial y$	0.80
$\partial w/\partial z$	0.80

Table 2. Correlations between the velocity gradient tensor fields  $(\partial u_i/\partial x_j)$  resulting from the scalar imaging velocimetry method and the exact DNS results for the  $Sc = 1$  case.

Results such as those in Figs. 3 and 4 demonstrate that, even in this limiting  $Sc = 1$  case, the scalar imaging velocimetry method is capable of yielding rather accurate results for the spatial structure of the full vector velocity fields and nine-component velocity



gradient tensor fields in turbulent flows. Since direct numerical simulations of turbulent mixing for  $Sc \gg 1$  scalars are beyond present computational reach, similarly detailed DNS studies of the accuracy of scalar imaging velocimetry for large  $Sc$  scalar field data are not possible. However we can anticipate that, owing to the excess scalar field information available in that case, extraction of the underlying velocity field is fundamentally more accurate for  $Sc \gg 1$  than at  $Sc = 1$ . Indeed, Ref. 1 demonstrated highly accurate extraction of velocity fields from large  $Sc$  turbulent flow data and a variety of test fields. Based on the relatively good accuracy demonstrated here for the extreme unity Schmidt number case in a full turbulent flow, on the fundamental improvement expected with increasing  $Sc$ , and on the results in Ref. 1, we expect that for  $Sc \gg 1$  data the method should be capable of accurately producing velocity and velocity gradient fields in turbulent flows.

#### 4. Tests of the SIV Technique

In this section, we apply the scalar imaging velocimetry technique to fully-resolved, four-dimensional, experimental data for  $Sc \gg 1$  scalar mixing in a turbulent shear flow, and from this extract the first experimental measurements of the underlying structure and dynamics of the full velocity gradient tensor field in a turbulent flow. The data used here are for the mixing of a dynamically passive  $Sc \approx 2075$  conserved scalar in the self-similar far field of an axisymmetric turbulent jet at outer-scale Reynolds number  $Re_\delta = 4,200$ . The experimental technique is described in detail in Sec. II.

An example of a typical two-dimensional spatial data plane from such a four-dimensional spatio-temporal data space is shown in Fig. 6a. Each such data plane has nominal dimensions of  $256 \times 256$  data points, and spans 2.2 strain-limited viscous diffusion lengthscales  $\lambda_v$  on each side, or approximately 1/25-th of the local jet width. Note that  $\lambda_v \approx 5.9 \cdot \lambda_K$ , where  $\lambda_K \equiv (\nu^3/\epsilon)^{1/4}$  is the classical Kolmogorov scale. With the finest scalar gradient lengthscale being  $\lambda_D = \lambda_v \cdot Sc^{-1/2}$ , these scalar field data are fully resolved in all three spatial dimensions. In particular, the in-plane pixel spacing is  $\Delta x = \Delta y = 107 \mu\text{m}$ , and the effective interplane spacing is  $\Delta z = 110 \mu\text{m}$ , while the local scalar diffusion lengthscale  $\lambda_D$  is  $239 \mu\text{m}$ . Further, the time separation between measurements at the same spatial point in two temporally successive three-dimensional spatial data volumes is  $\Delta t = 0.0532$  sec. This compares with the local scalar gradient advection timescale  $\lambda_D/\mu$  of 0.0848 sec, indicating that the data are essentially resolved in time as well. This level of resolution, together with the high signal quality attained, allows accurate differentiation of the measured scalar field data simultaneously in all three space dimensions and in time. Examples of typical resulting  $\partial\zeta/\partial t$ ,  $\nabla\zeta$ , and  $\nabla^2\zeta$  fields are shown in Figs. 6b-d. All derivatives are obtained here by direct linear central differencing on the measured scalar field data, with no explicit smoothing or filtering applied. Notice that even the second derivatives in Fig. 6d are relatively free of the effects of noise. The variational nature of the implementation outlined in Section II for scalar imaging velocimetry should make the results obtained relatively insensitive to the errors that even this low level of noise introduces in (1).

Data of the type in Fig. 6, together with the scalar imaging velocimetry method in (3)-(12), allows the underlying fluid velocity field  $\mathbf{u}(\mathbf{x};t)$  throughout the four-dimensional data space to be found. Since  $Sc \approx 2075$  in these measurements, the ratio of the finest gradient lengthscales in the velocity and scalar fields is  $\lambda_v/\lambda_D \approx 15$ , and as a consequence

measurements such as these that fully-resolve the scalar field are highly oversampled for the velocity field. For this reason we subsample each of the scalar derivative planes in the four-dimensional data space to  $64 \times 64$  points. In that case, scalar field is still oversampled by roughly a factor of four, but the computational work required to find the velocity field has been reduced considerably. The resulting  $u$  and  $w$  vectors each contain 61,440 elements, and the  $A$  matrix contains approximately  $3.8 (10^9)$  elements, of which  $1.23 (10^6)$  are non-zero. The same (non-optimized) Jacobi iteration algorithm used in Section III then typically requires about 20 minutes to solve the linear system for the velocity field  $u(x;t)$  in (12) at each time  $t$ .

#### A. Vector velocity fields

Fig. 7 shows the resulting  $u$ ,  $v$ , and  $w$  components of the velocity vector field in the same scalar field data plane shown in Fig. 6. For the coordinate orientation used,  $u$  gives the radial component,  $v$  the streamwise component, and  $w$  the azimuthal (out of plane) component. The mean velocity has been subtracted from these components, so that the instantaneous fluctuation values are shown. Note that the apparent lengthscale characteristics of the velocity gradients in these results is quite consistent with the estimate given above: i.e. each data plane spans approximately 2.2 velocity gradient lengths in each direction. It should be noted that full three-component velocity vector field measurements such as these have not previously been available, and thus it is not common to present velocity field information in the form shown in Fig. 7. More typically, experimental velocity component fields are presented as projections of the local vectors into a measurement plane. For this reason, the data from Fig. 7 are shown in this manner in Fig. 8, where the  $(u,v)$  and  $(u,w)$  projections at each point in that particular plane are given.

It is apparent from the data in Figs. 7 and 8 that, owing to the large  $Sc$  involved, these measurements allow examination of the velocity field at the dissipative scales of turbulent flows. Results for the full vector velocity field over a larger range of lengthscales requires similarly resolved scalar field measurements at a significantly lower value of  $Sc$ , since  $\lambda_v/\lambda_D = Sc^{1/2}$ . The class of scalars for which practical measurements of the type required here are feasible is quite limited. The most promising among these appears to be the temperature field, which can be measured via the temperature-dependent collisional de-excitation rate of certain laser dyes (Dahm, Su & Frederiksen 1993). In that case  $Sc \approx 7$ , and thus the range of lengthscales in the velocity field accessible to the measurements is over 17 times larger than in Figs. 7 and 8. This would allow spatial measurements over lengthscales extending from the dissipative range into the inertial range. The prospects for such measurements is discussed further in Section V. For the moment, we concentrate on the velocity gradient fields associated with vector velocity field measure-

ments of the type in Figs. 7 and 8.

### B. *Velocity gradient tensor fields*

Velocity vector field measurements in any given three-dimensional spatial data volume, formed from parallel planes of the type in Figs. 7 and 8, allow simultaneous differentiation of each of the  $u$ ,  $v$ , and  $w$  components in  $x$ ,  $y$ , and  $z$  to determine the full nine-component velocity gradient tensor. Of particular interest for dynamical studies of the small scales of turbulence are the symmetric and antisymmetric parts of this tensor. Fig. 9 shows the (symmetric) strain rate tensor field components  $\epsilon_{ij}(\mathbf{x};t)$  in the same plane for which results were given in Figs. 6-8. Similarly, the vorticity vector field components  $\omega_i(\mathbf{x};t)$  in the same plane, formed from the antisymmetric velocity gradient tensor components, are shown in Fig. 10. From these individual velocity and velocity gradient component fields, dynamical quantities of interest such as the kinetic energy density field  $k(\mathbf{x};t) \equiv \frac{1}{2} \mathbf{u} \cdot \mathbf{u}(\mathbf{x};t)$  in Fig. 10a, the kinetic energy dissipation rate field  $\Phi(\mathbf{x};t) \equiv 2\nu \epsilon_{ij} \epsilon_{ij}(\mathbf{x};t)$  in Fig. 10b, and the enstrophy field  $W(\mathbf{x};t) \equiv \omega_i \omega_i(\mathbf{x};t)$  in Fig. 10c can be examined. Moreover, interactions between the symmetric and antisymmetric tensor components, such as the enstrophy production rate  $\Omega(\mathbf{x};t) \equiv \omega_i \epsilon_{ij} \omega_j(\mathbf{x};t)$  and the scalar dissipation production rate  $Z(\mathbf{x};t) \equiv \nabla \zeta_i \epsilon_{ij} \nabla \zeta_j(\mathbf{x};t)$ , are of particular dynamical interest and can be examined with very high resolution from measurements such as those in Figs. 6-9.

Studies of all these fields require knowledge of the full nine-component velocity gradient tensor field, as in Figs. 9 and 10. Such laboratory measurements of the velocity gradient field on the small scales of a turbulent flow have not previously been possible. There are four key aspects of the present measurements that collectively make them unique. Firstly, the scalar imaging velocimetry measurements demonstrated here, giving the velocity gradient tensor at the small scales of turbulent flows, are fully-resolved. Previous measurements with similar aims<sup>10-20</sup> have been limited to significantly coarser resolution levels, which thereby at least partially corrupt the gradient tensor components, since these are highly sensitive to resolution. [It should be noted that the experimentally measured velocity gradient fields in Figs. 7 and 8 are rather highly resolved even in comparison with those typically obtained from direct numerical simulation (DNS) studies of the small scales of turbulence. In general, resolution limitations in such simulations, coupled with the need to supply initial conditions with a sufficient number of excited modes, allows only comparatively few grid points or spectral modes across the smallest velocity gradient lengthscale. By comparison, in these laboratory measurements the interactions between gradient lengthscales accessible to the measurement and all larger scales occur naturally, allowing a much larger number of points across the finest gradient lengthscale. This is evident by comparing the fields in Figs. 6-10 with typical DNS fields.] Secondly,

the present measurements are entirely noninvasive, in contrast to earlier measurements based on multiple hot wire probes. As a consequence, the measurements themselves do not alter the quantities being measured. Thirdly, unlike most previous measurements of the gradient tensor components, the present scalar imaging velocimetry technique inherently produces all nine components of this tensor. Most previous probe-based measurements as well as optically-based techniques have been limited to some subset of these. Finally, in contrast to probe-based methods, which are inherently single-point techniques producing time-series data for the gradient components at a single point, the present measurements produce these at a very large number of points sufficiently closely spaced in both space and time to define the continuum fields. These are thus field measurements, as opposed to point measurements, and they thereby allow experimental examination not only of statistics of the velocity gradient components, but of the underlying spatiotemporal structure and dynamics in these dynamical fields at the small scales of turbulence.

### C. *Temporal evolution of the velocity gradient field*

Results presented in the previous sections have been for the spatial structure of the velocity gradient tensor field at a fixed instant in time. However, the four-dimensional nature of the scalar field data on which these velocity field measurements are based allows the inversion in (12) to be performed at each time step  $\Delta t$ . Accordingly, the time evolution of any of the fields in the previous section can be examined by repeating the inversion at the requisite times and assembling the fields of interest in time as shown, for instance, in Fig. 11. This figure presents the time-varying kinetic energy density field  $k(\mathbf{x}, t)$  and the corresponding kinetic energy dissipation rate field  $\Phi(\mathbf{x}, t)$  in the same spatial plane for which results were shown in Figs. 6-10, at 10 sequential instants in time. The time axis is measured in the inner variable  $(t \cdot \nu/\lambda_v^2)$ , where  $t = 0$  corresponds to the instant for which the results were shown in Figs. 6-10.

Note that, just as the fully-resolved  $Sc \gg 1$  scalar field data oversamples the velocity field in space, the requisite time resolution demanded of the scalar field measurements leads to a  $\Delta t$  between successive three-dimensional spatial data volumes that is smaller than needed to fully resolve the time evolution of  $\mathbf{u}(\mathbf{x}, t)$ . The results in Fig. 11 are thus shown at time intervals spaced  $3 \Delta t$  apart. Clearly the structure in these planes is well correlated from one time step to the next, and further, the planes describe a clear temporal evolution of the flow. This is significant because, for this spacing in time, there is *no* common scalar field data involved in any of these time steps. No two planes share scalar field information in the scalar imaging velocimetry implementation in (3)-(12). Thus noise in the scalar field data is uncorrelated from one time step to the next. As a consequence, if the formulation implemented here to find the velocity field were sensitive to

noise, there would be no *a priori* reason why the same field at two successive times in Fig. 11 should demonstrate a strong correlation or a clear evolution. The strong correlation of the results therefore must be ascribed to the fundamental well-posedness of the variational formulation. Moreover, while the results shown are spaced  $3 \Delta t$  apart, the availability of the velocity gradient field components at all intermediate times permits accurate differentiation of the results to yield the detailed time evolution of the fine scales of turbulent flows.

#### D. Concluding remarks

The experimental access to the spatial structure and time evolution of the full nine-component velocity gradient tensor which this scalar imaging velocimetry technique offers allows a level of detailed investigation of the dynamics of the small scales of turbulent flows that has previously been conceivable only through DNS studies. These experimental results actually provide higher resolution of the fine scales than is currently possible by such direct numerical simulations. Moreover, as demonstrated here, the availability of practical experimental techniques for measuring the requisite scalar field information. The velocity fields which result from application of the scalar imaging velocimetry technique to this scalar field measurement technique are thus currently well suited to investigations of the fine structure and dynamics of the inner scales of turbulent flows.

Comparisons of the DNS and experimental scalar fields (Figs. 1 and 7, respectively) and the corresponding velocity fields (Figs. 4, 9) demonstrate clearly the differing character of the low and high Schmidt number limits. While the experimental scalar field appears to have finer characteristic length scales than the DNS scalar field, the DNS velocity field clearly has much finer length scales than does the experimental field. In particular, comparison of the fields emphasizes the variance in characteristic velocity and scalar lengthscales, which goes as  $Sc^{1/2}$ , and also shows the degree to which the  $Sc = 1$  limit is a demanding one for the SIV technique.

At present, scalar field data which is sufficiently resolved to permit application of the scalar imaging velocimetry technique is only available for flows with  $Sc \gg 1$ . Thus the realm of  $Sc \approx 1$  flows, e.g. the gas phase flows of particular interest in combustion applications, remains inaccessible by the fully resolved scalar field measurements necessary for this velocimetry method. However, the lack of suitable scalar field diagnostics is the only limitation; as shown in §4, fully resolved  $Sc \approx 1$  scalar field information is fully amenable to the scalar imaging velocimetry technique.

Mention possibility of using T-field imaging (refer to Dahm, Su & Frederiksen 1993 Lisbon submitted) for  $Sc = 7$ , giving 17 x larger view of flow field  $SQRT(2075/7) = 17.2$ . Preliminary results suggest that this is feasible using the same approach used here

to obtain measurements of the dissipative scales of motion in turbulent flows. That would permit experimental measurements of the full velocity gradient tensor over lengthscales extending from the dissipative scales into the inertial range, thereby allowing laboratory studies of subgrid scale dynamics.

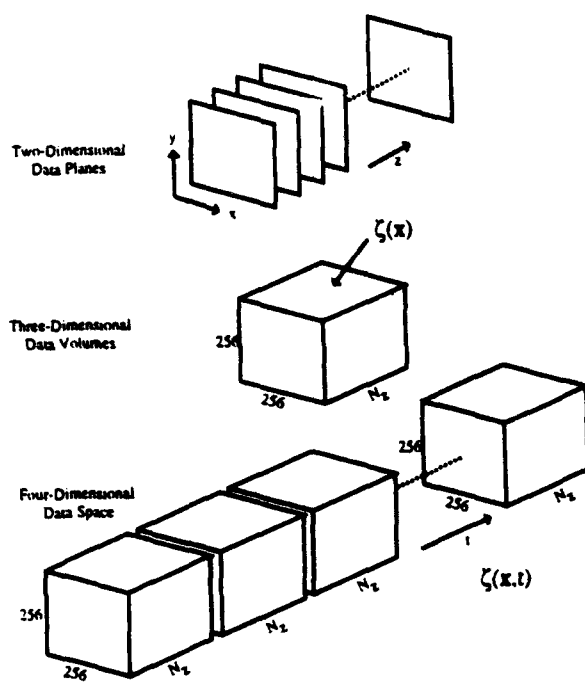


Figure 1. Schematic of the data acquisition process, showing the progression from  $256 \times 256$  data planes, to  $256 \times 256 \times N_z$  three-dimensional data volumes, resulting in the full four-dimensional data set. The full data space contains over 3 billion point measurements of the scalar field.



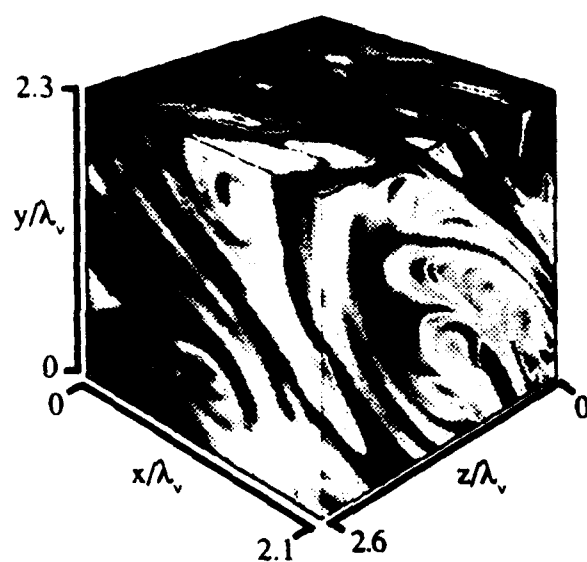


Figure 2. A three-dimensional data volume of the type described in Refs. 35, 36. The outer scale Reynolds number is  $Re\delta = 3700$ . Red represents the highest scalar concentration value in the volume, while blue denotes pure ambient fluid.

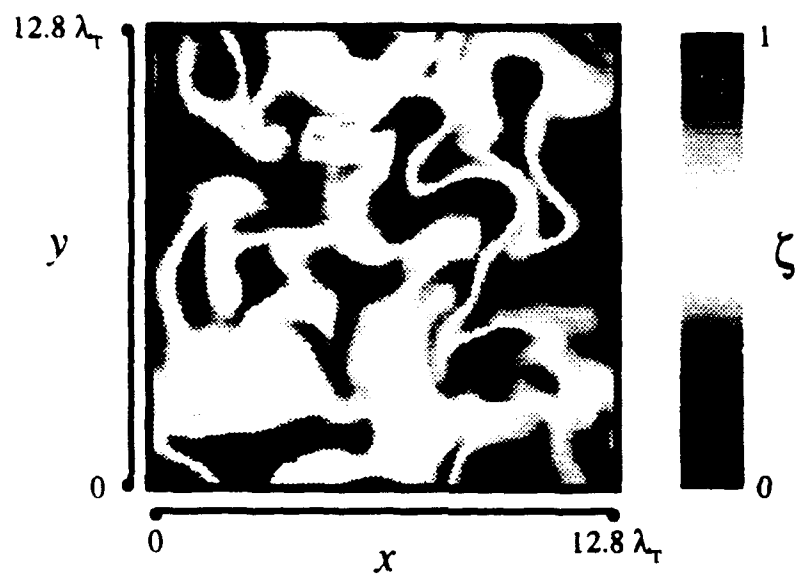


Figure 3. Scalar field information from a direct numerical simulation of turbulent mixing at  $Sc = 1$ . (a) A sample data plane.

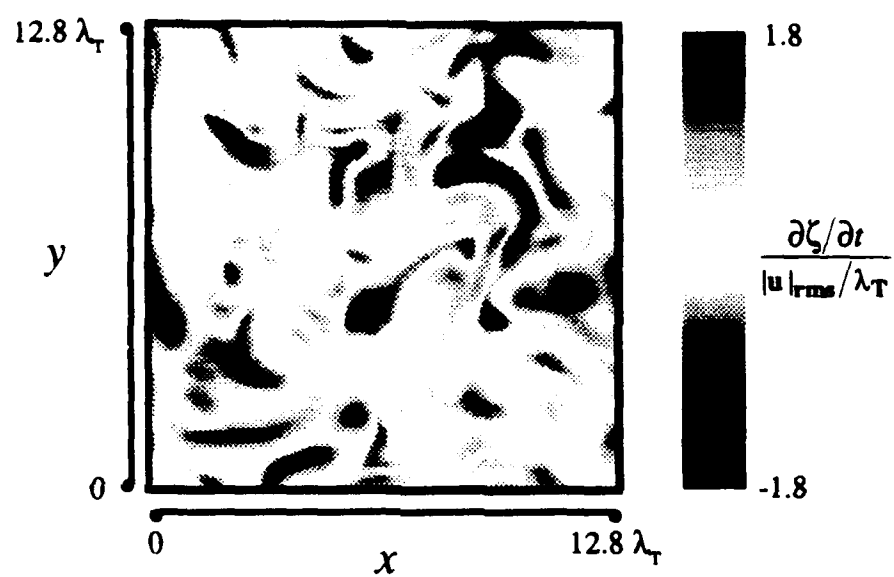


Fig. 3b. The time derivative  $\partial\zeta/\partial t$  for the plane in (a).

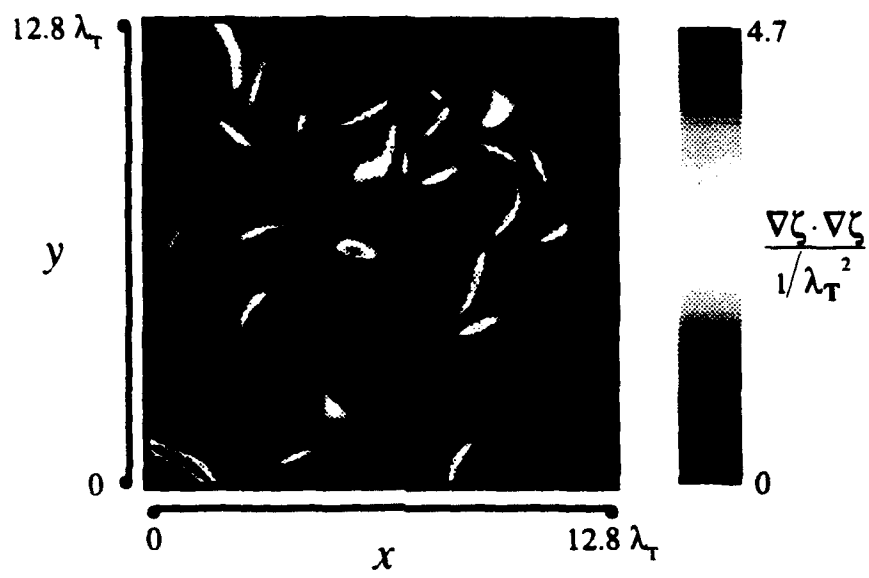


Fig. 3c. The scalar energy dissipation  $\nabla \zeta \cdot \nabla \zeta$ .

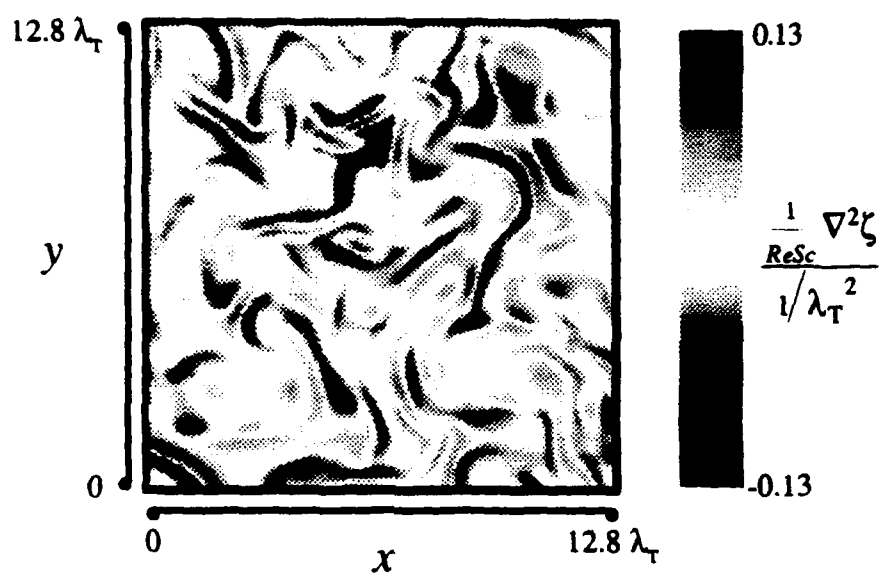


Fig. 3d. The scalar field diffusion term  $(1/ReSc)\nabla^2\zeta$ .

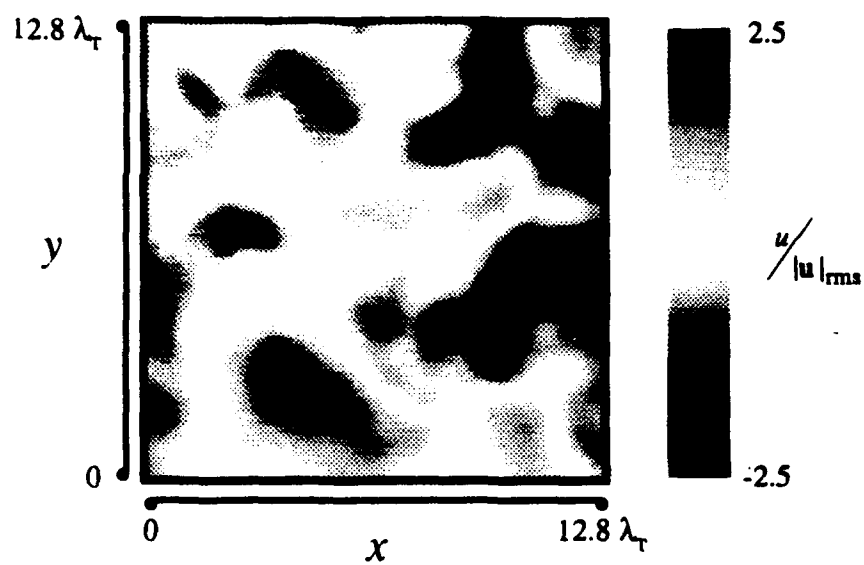


Figure 4. Comparisons of SIV velocity results with known DNS fields, for the scalar field information in Fig. 3. (a) The  $u$ -component of the velocity, from SIV.

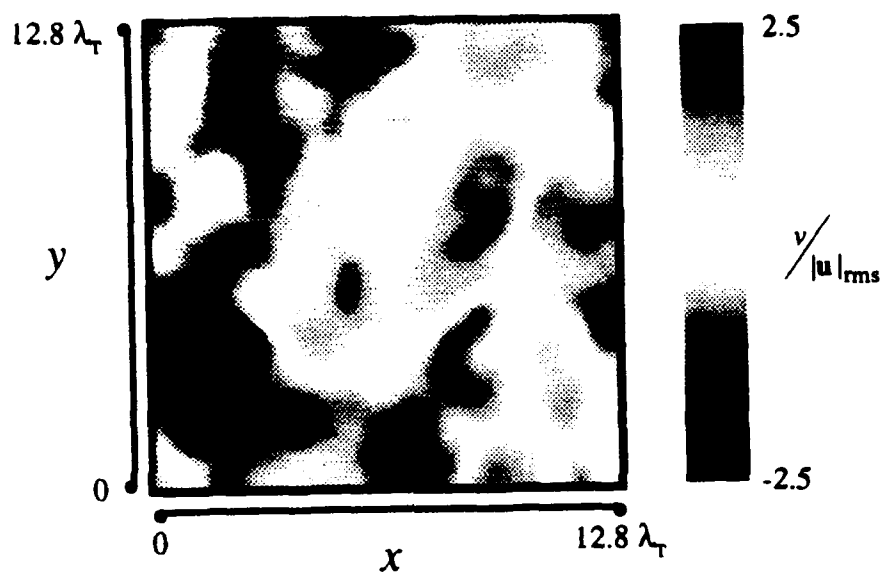


Fig. 4b.  $v$ -component, SIV.

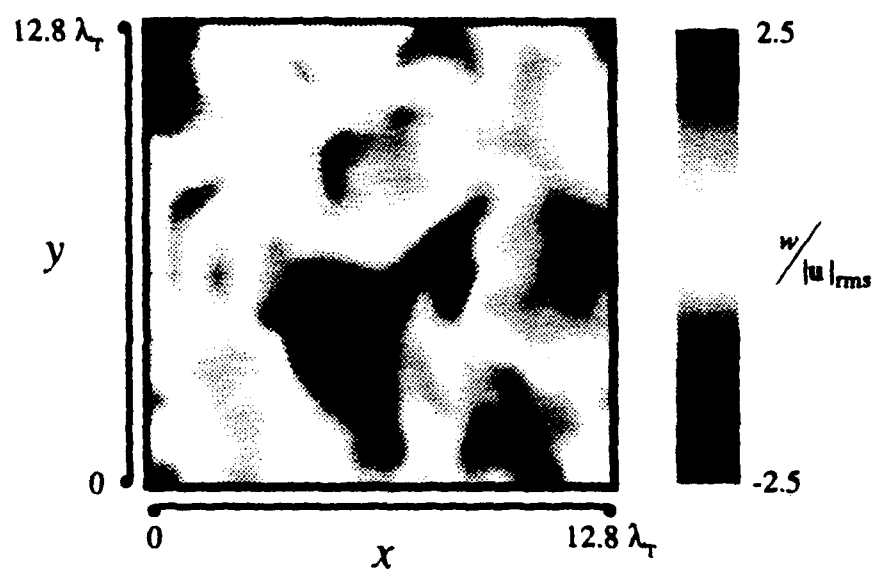


Fig. 4c. w-component, SIV.



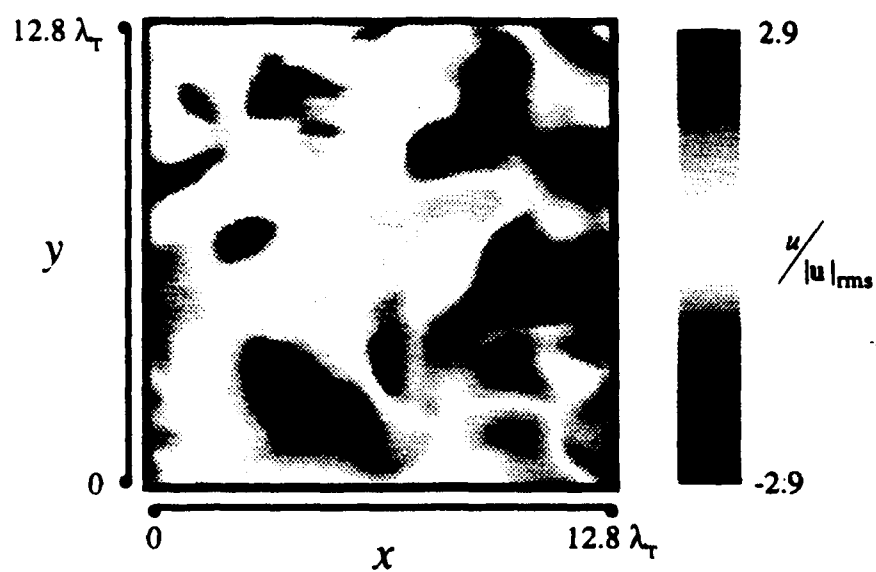


Fig. 4d. The actual DNS  $u$ -component field.

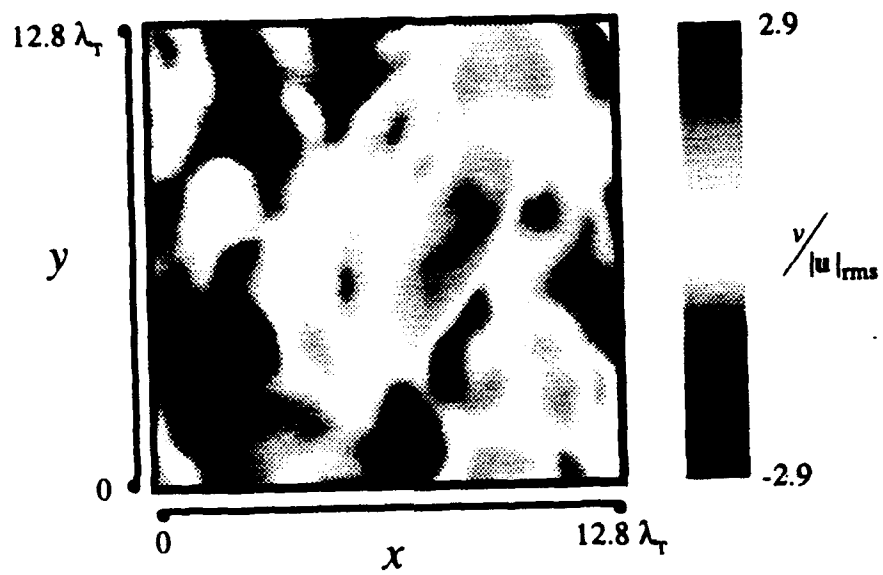


Fig. 4e. v-component, DNS.

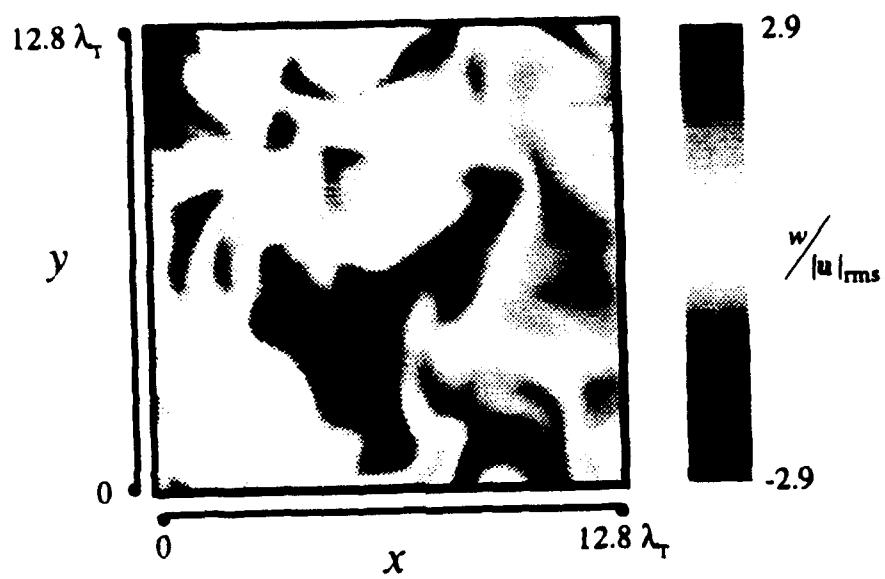


Fig. 4f.  $w$ -component, DNS.

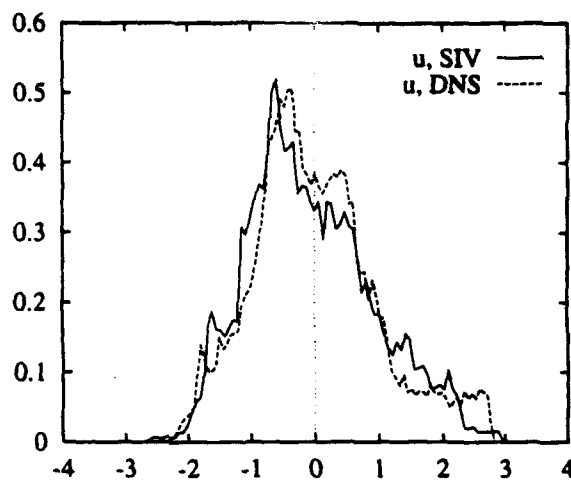


Figure 5. Comparisons of the pdf's of velocity component values  $u_i/u_{i,rms}$  for the SIV results and the DNS fields of Fig. 4. (a)  $u$ -component.

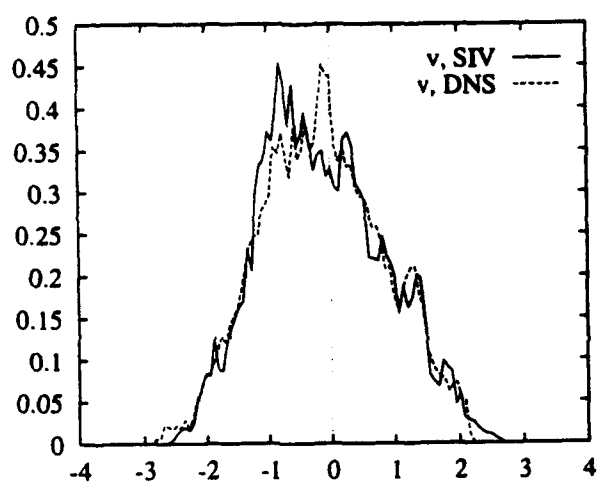


Fig. 5b.  $v$ -component.

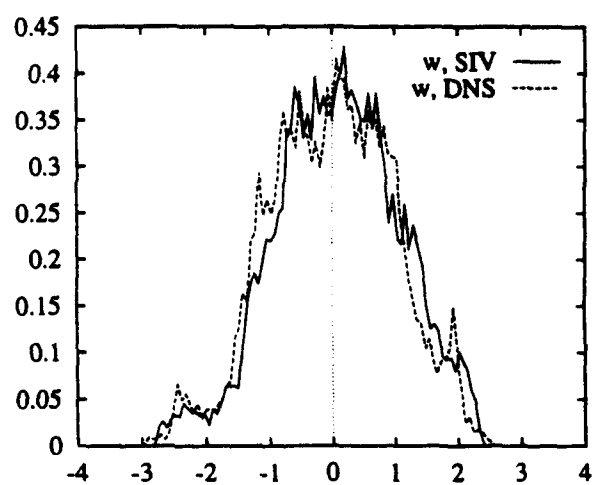


Fig. 5c.  $w$ -component.

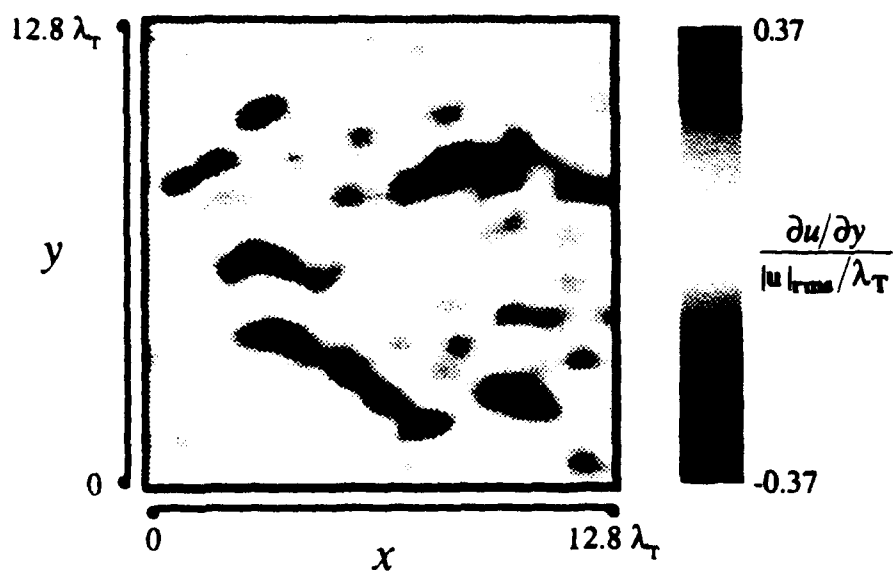


Figure 6. Velocity gradient component fields, for both the SIV results and the DNS fields of Fig. 4. (a) The  $\partial u / \partial y$  field from SIV.

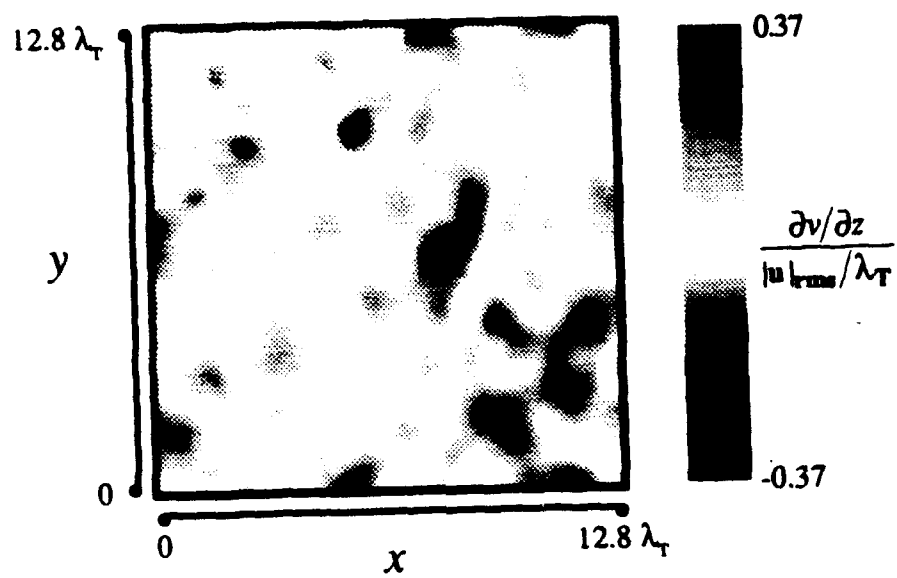


Fig. 6b.  $\partial v / \partial z$ , SIV.



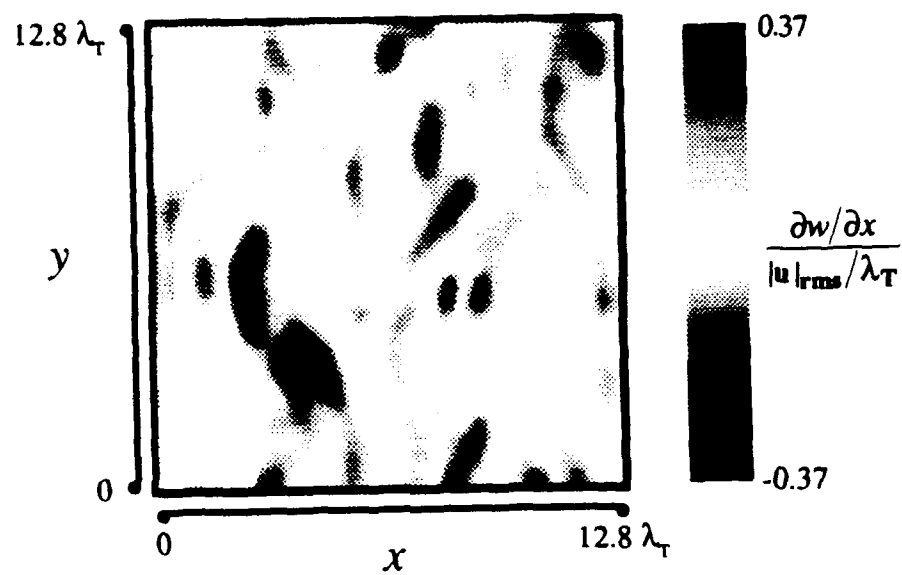


Fig. 6c.  $\partial w / \partial x$ , SIV.

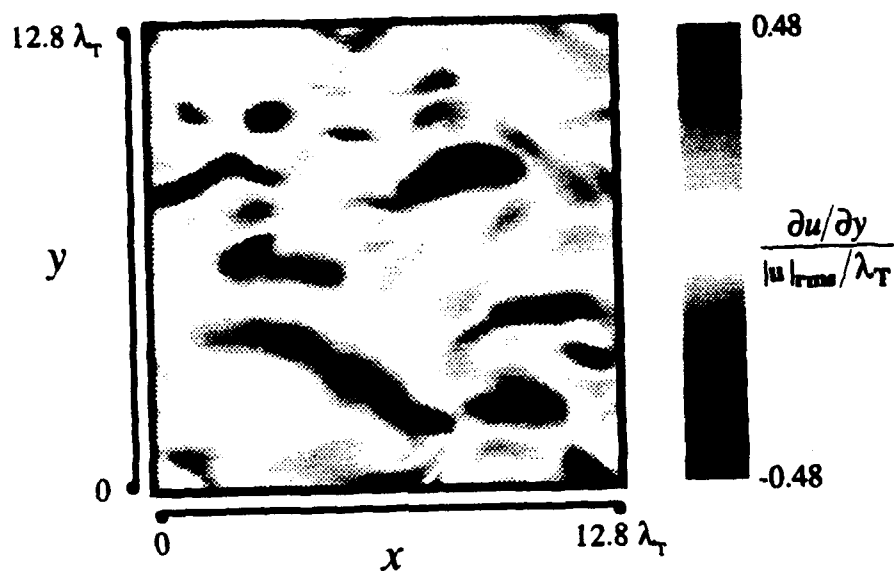


Fig. 6d. The actual DNS  $\partial u / \partial y$  field.

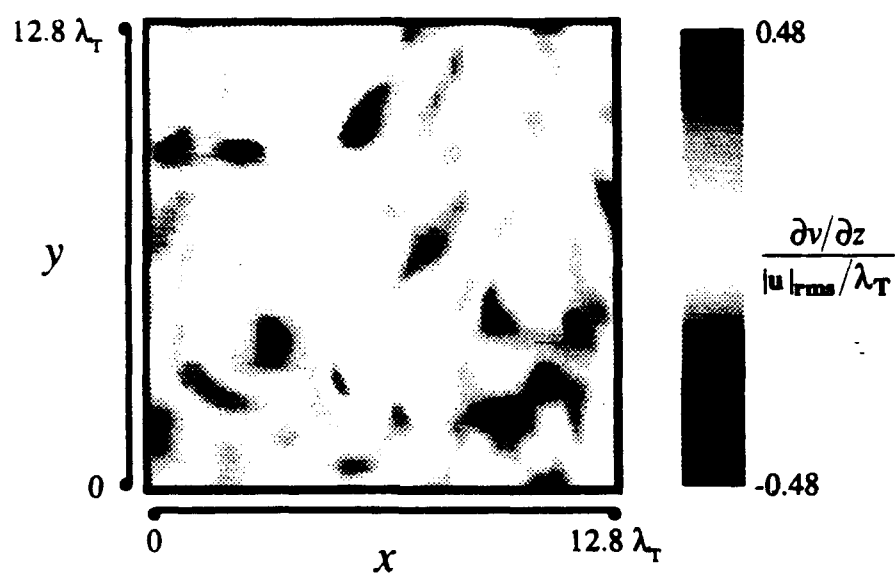


Fig. 6e.  $\partial v / \partial z$ , DNS.

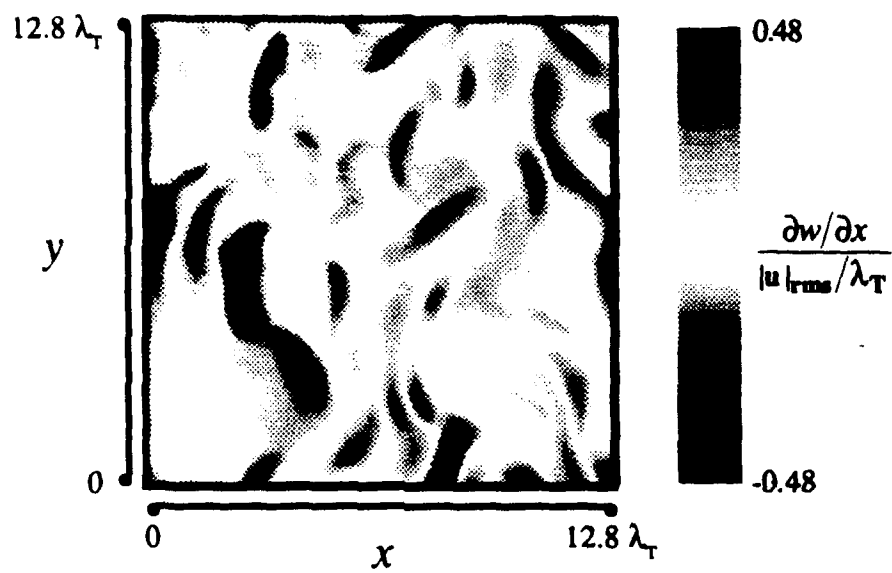


Fig. 6f.  $\partial w / \partial x$ , DNS.

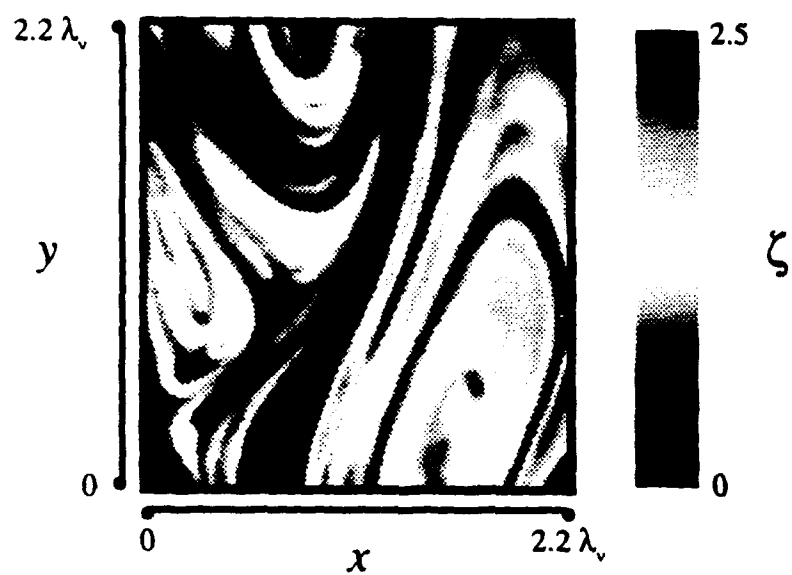


Figure 7. Scalar field information from an experimental turbulent flow at  $Sc \approx 2075$ . The acquisition scheme is described in Refs. 34-37.  
 (a) A sample data plane.

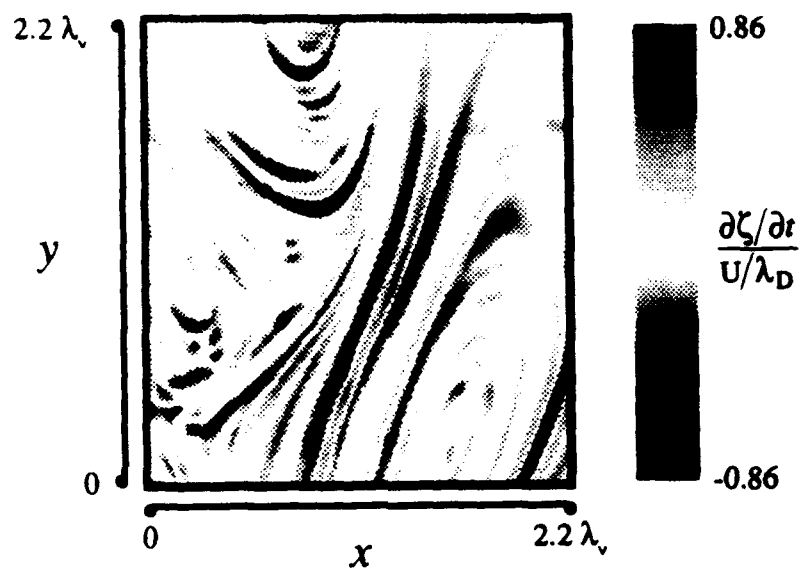


Fig. 7b. The time derivative  $\partial\zeta/\partial t$  for the plane in (a).

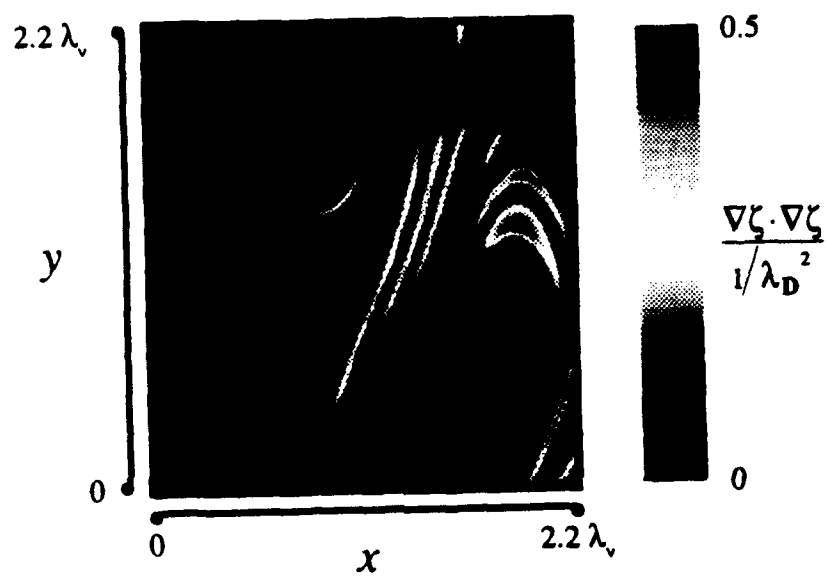


Fig. 7c. The scalar energy dissipation  $\nabla \zeta \cdot \nabla \zeta$ .

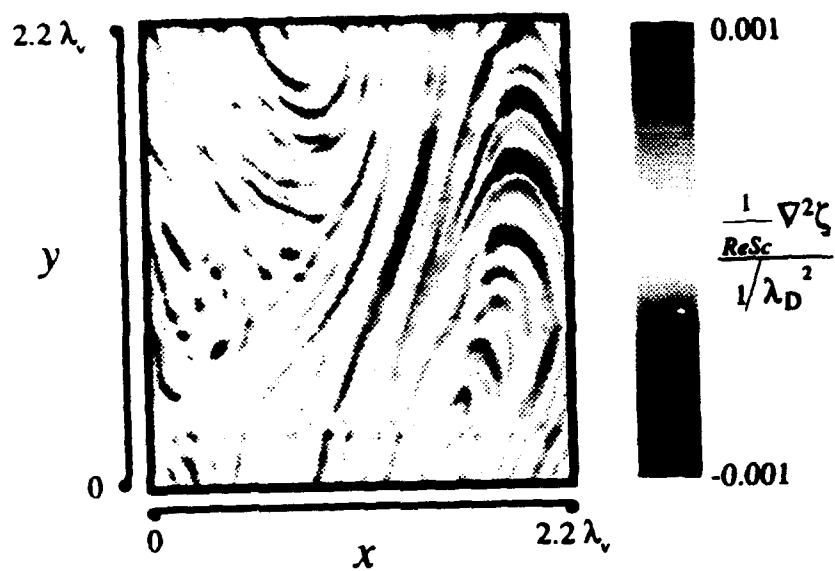


Fig. 7d. The scalar field diffusion term  $(1/ReSc)\nabla^2\zeta$ .



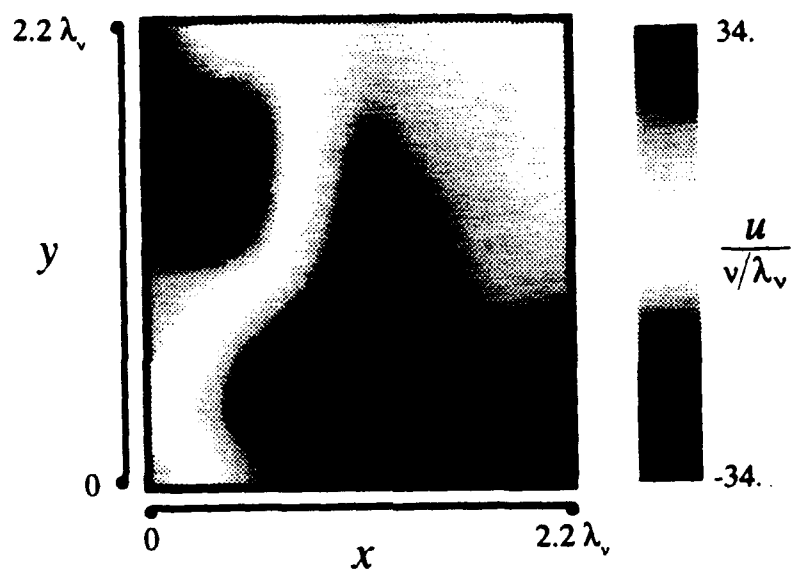


Figure 8. SIV results for the velocity field in a turbulent flow at  $Sc \approx 2075$ , from the scalar field information in Fig. 7. (a)  $u$ -component.

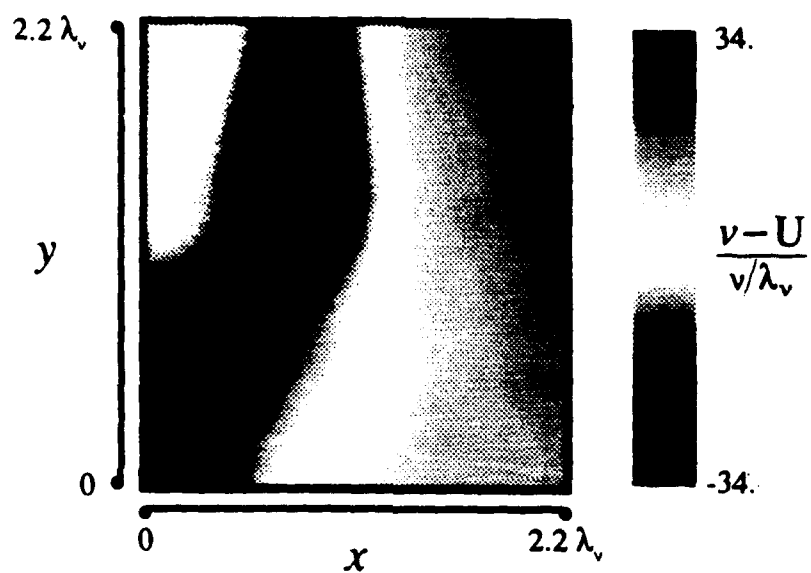


Fig. 8b. The  $v$ -component, with the mean streamwise component having been subtracted out.

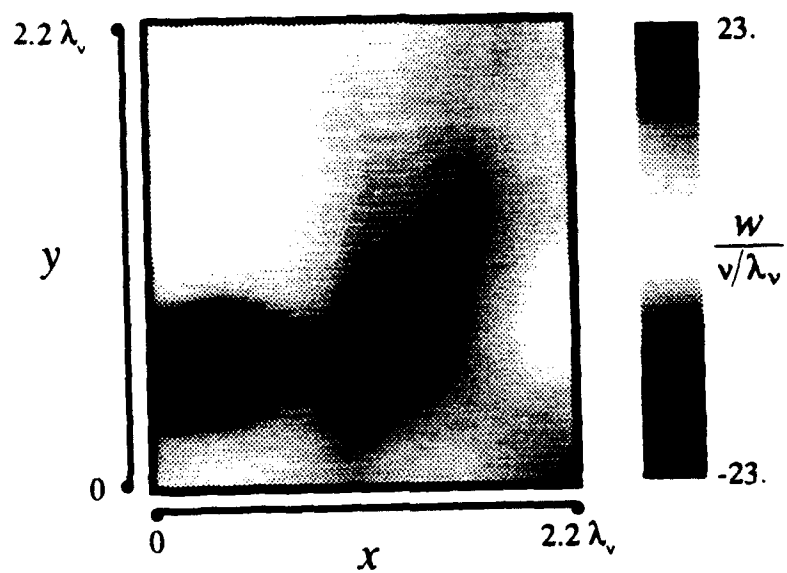


Fig. 8c.  $w$ -component.

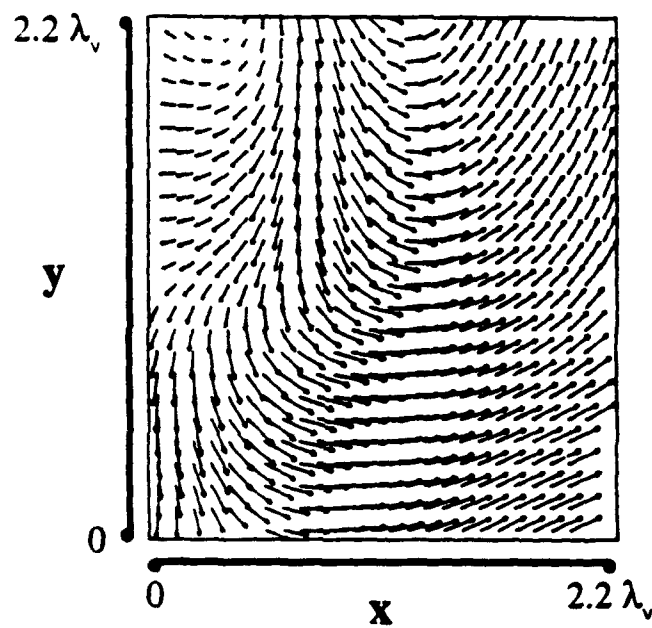


Figure 9. Projections of the SIV results of Fig. 8 onto two-dimensional planes. (a) The  $u$ - and  $v$ -components.

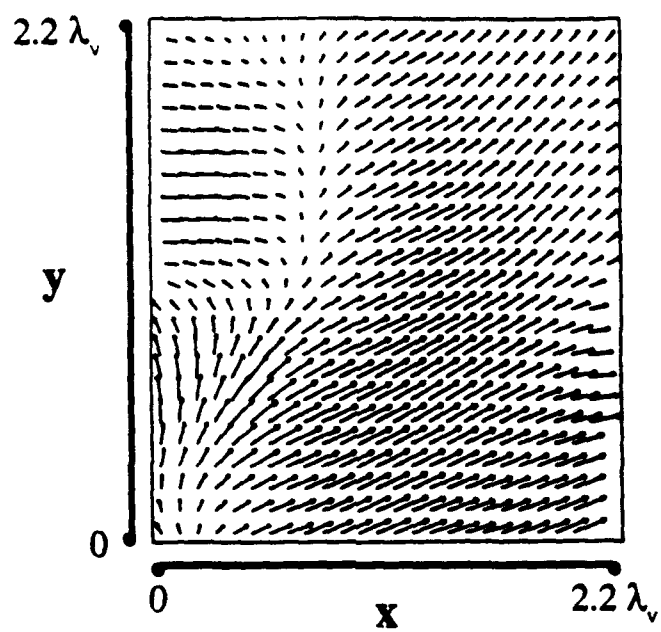


Fig. 9b. The  $u$ - and  $w$ - components.

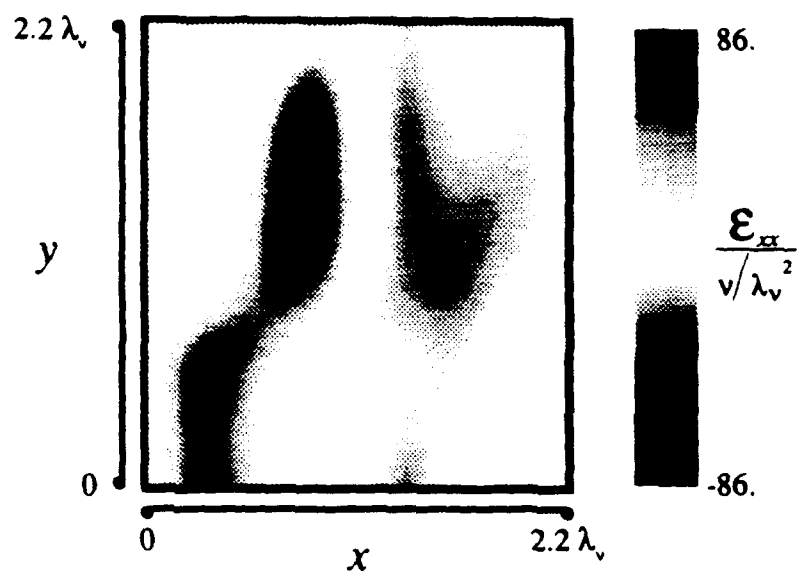


Figure 10. Components of the velocity gradient tensor, from the SIV results of Fig. 8. (a) The  $\epsilon_{xx}$  field.

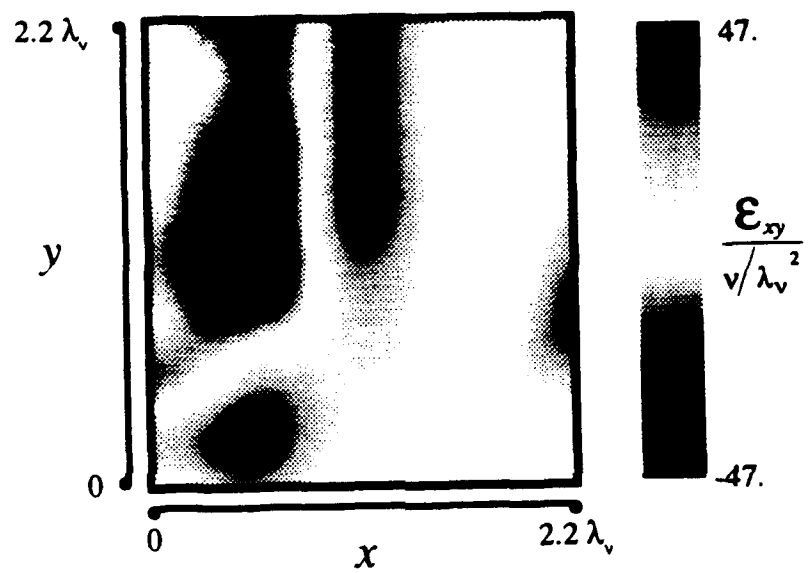


Fig 10b.  $\epsilon_{xy}$ .

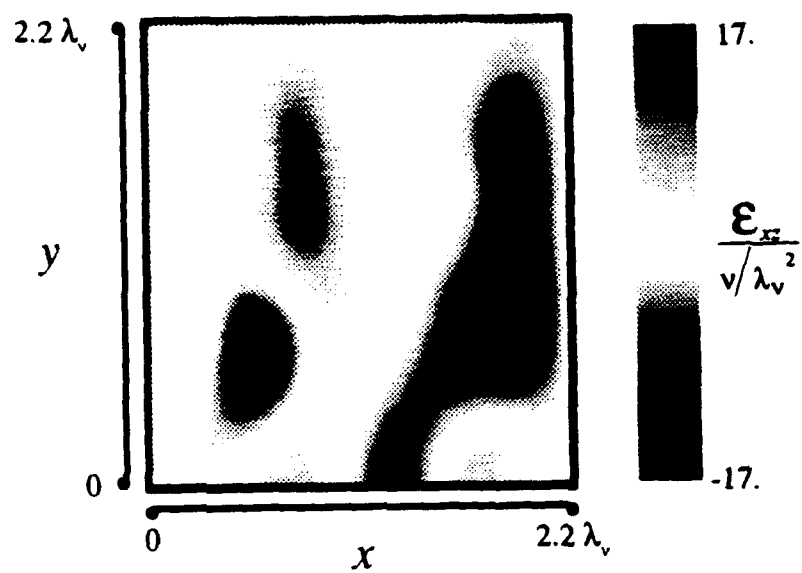


Fig. 10c.  $\epsilon_{xz}$ .



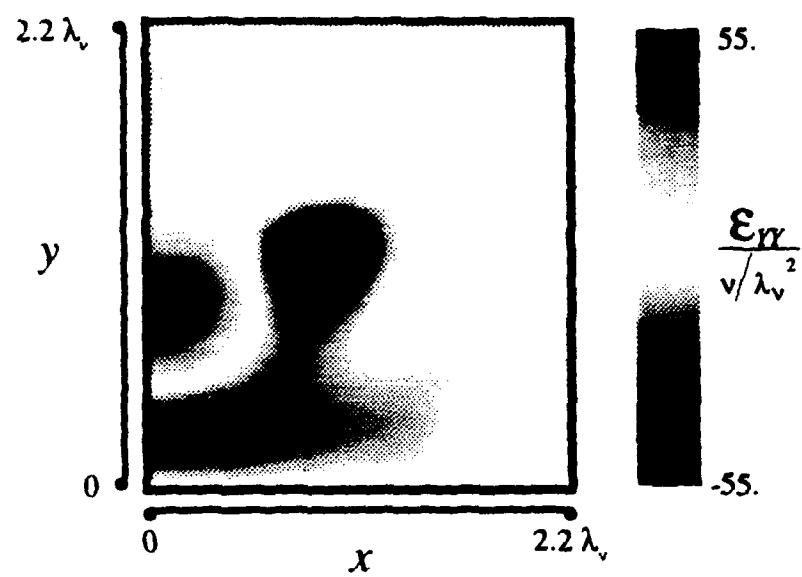


Fig. 10d.  $\epsilon_{yy}$ .

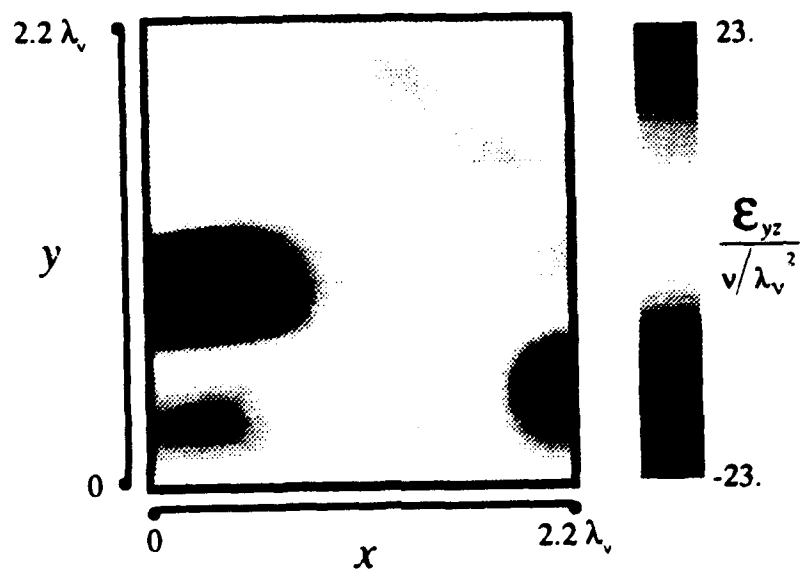


Fig. 10e.  $\epsilon_{yz}$ .

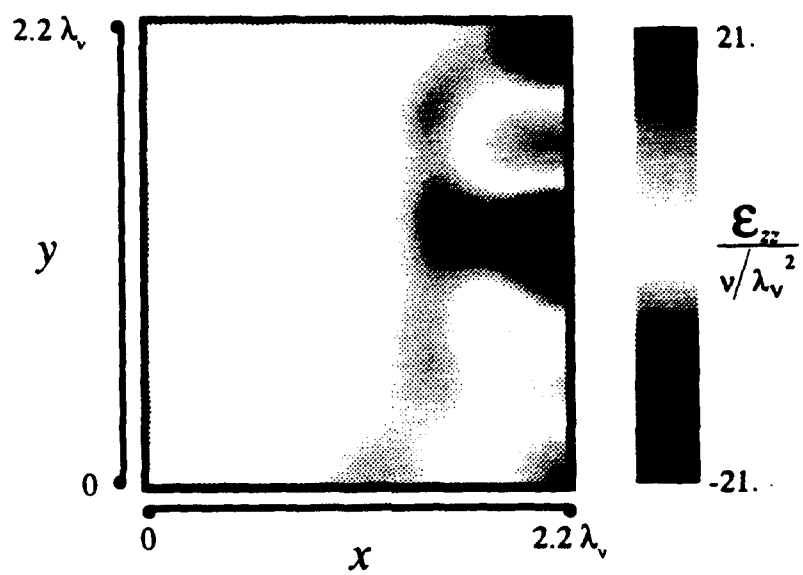


Fig. 10f.  $\epsilon_{zz}$ .

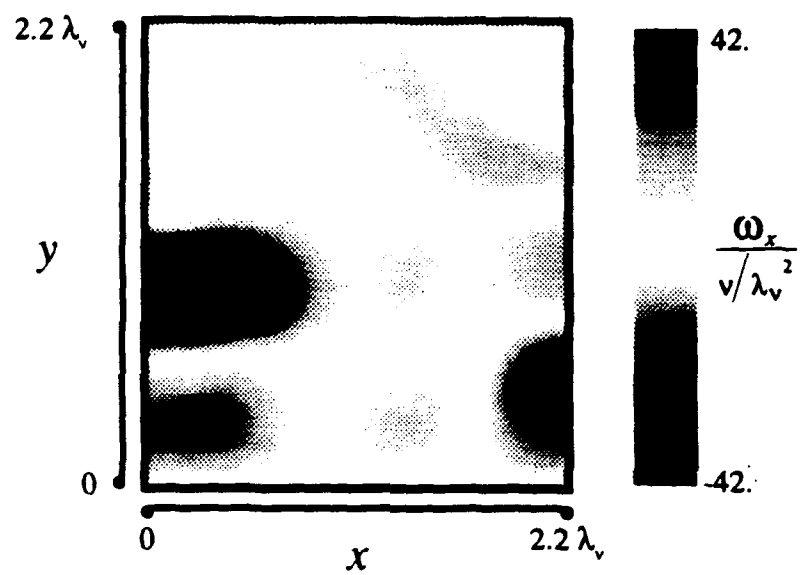


Figure 11. Components of the vorticity vector  $\omega$ , from the SIV results of Fig. 8. (a)  $\omega_x$ .

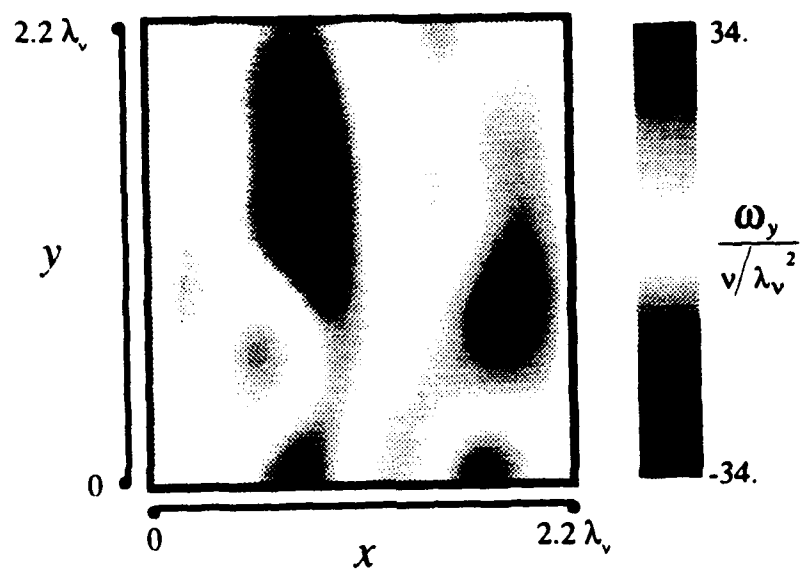


Fig. 11b.  $\omega_y$ .

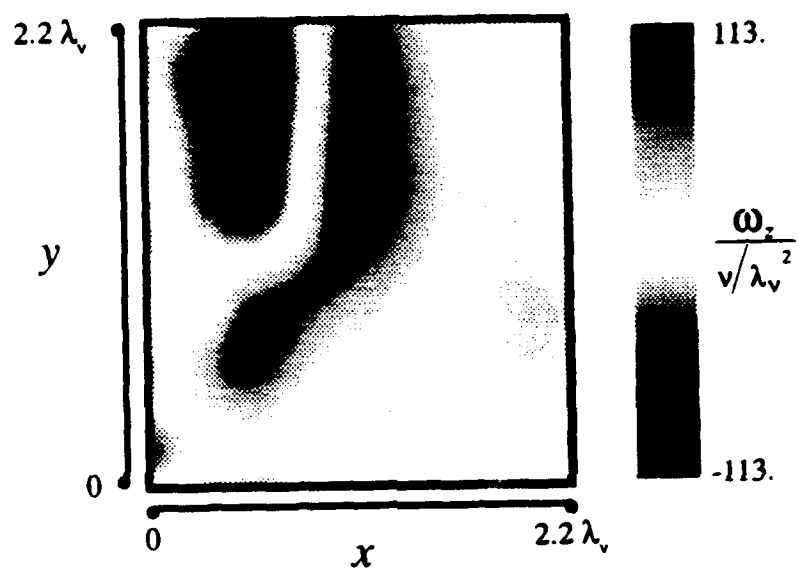


Fig. 11c.  $\omega_z$ .

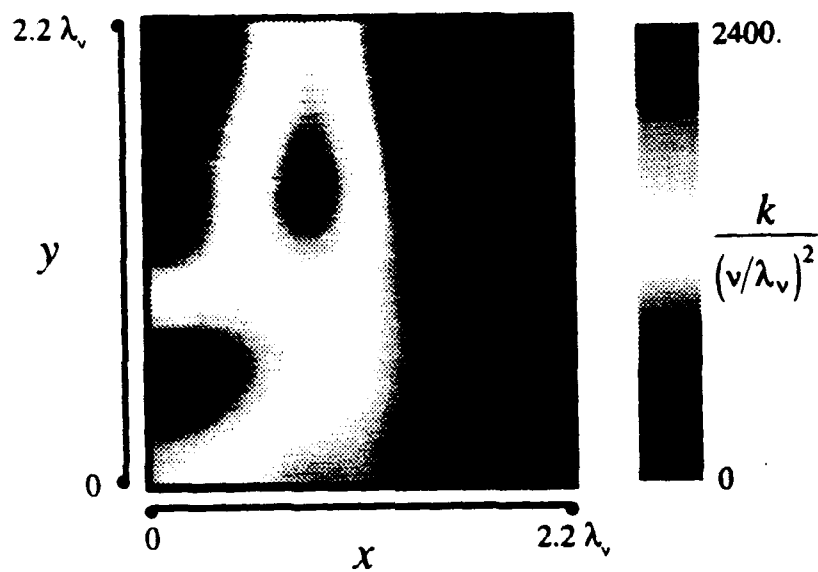


Figure 12. Dynamical quantities from the SIV results of Fig. 8, and the velocity gradients of Fig. 10. (a) The kinetic energy field  $k(x,t)$ .

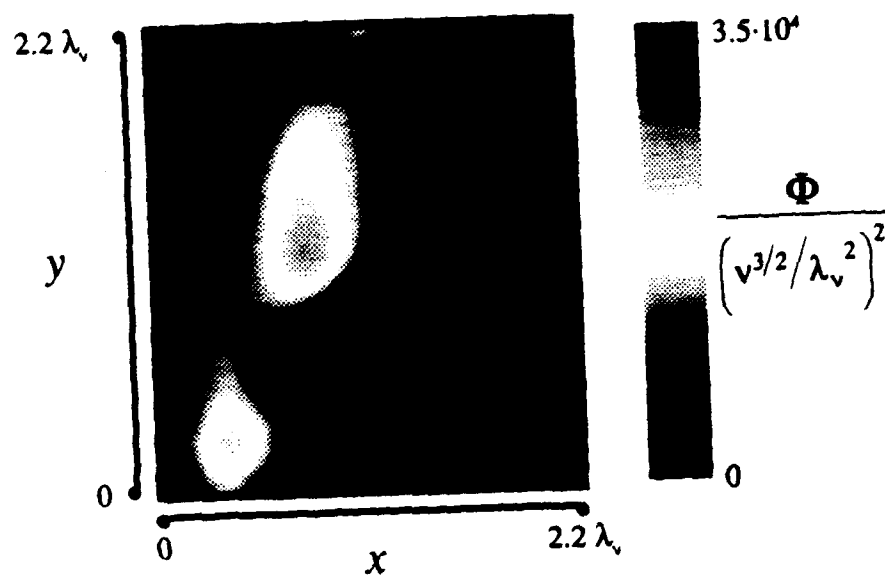


Fig. 12b. The kinetic energy dissipation rate field  $\Phi(x, t)$ .



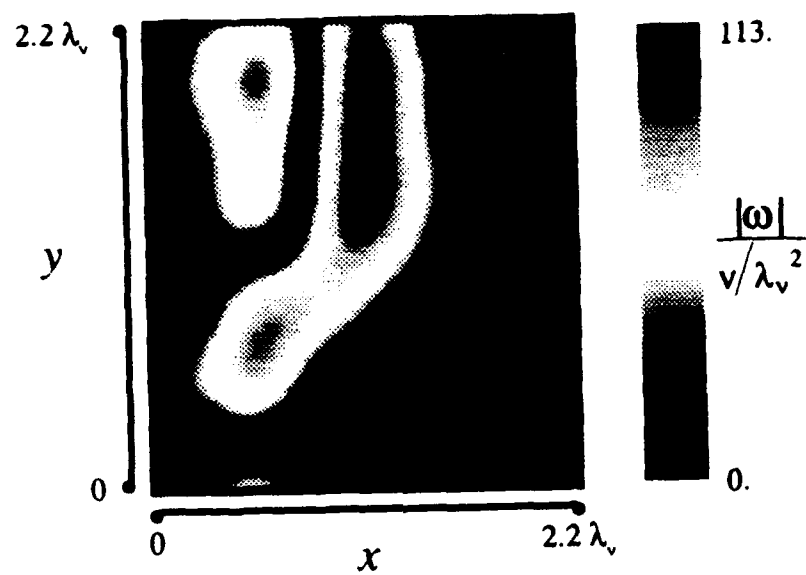


Fig. 12c. The vorticity magnitude  $|\omega|(\mathbf{x}, t)$ .

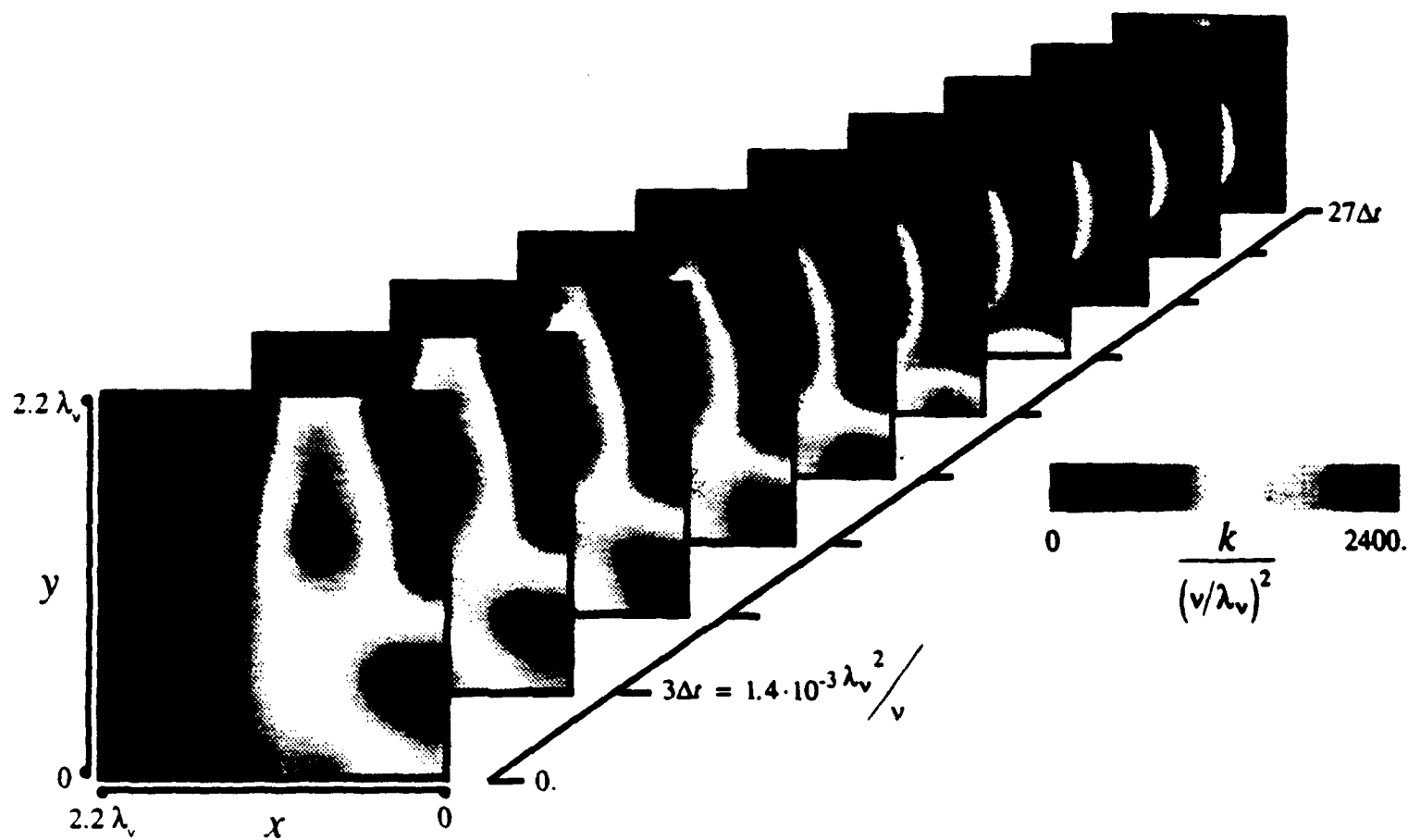


Figure 13. Examples of time evolution information available from SIV studies. (a) Evolution of the kinetic energy field  $k(x,t)$ .

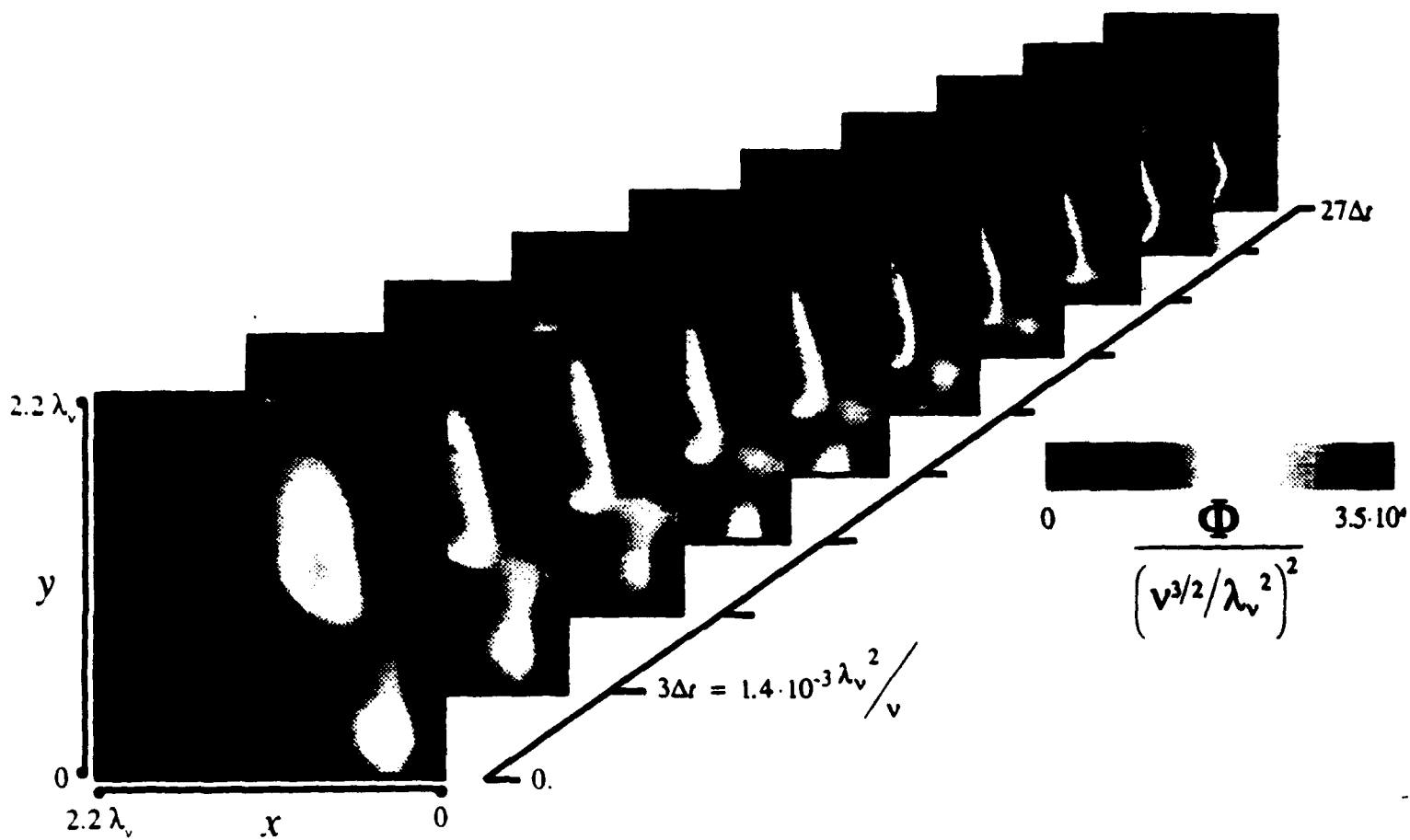


Fig. 13b. Evolution of the kinetic energy dissipation rate field  $\Phi(x,t)$ .

## References

- [1] Dahm, W.J.A., Su, L.K. & Southerland, K.B. (1992) A scalar imaging velocimetry technique for fully resolved four-dimensional vector velocity field measurements in turbulent flows. *Phys. Fluids A* 4, 2191.
- [2] Dahm, W.J.A., Su, L.K. & Southerland, K.B. (1992) Scalar imaging velocimetry measurements of vector velocity, vorticity and tensor strain rate fields in turbulent flows. Proceedings of the 6th International Symposium on Applications of Lasers in Fluid Mechanics, pp. 3.1.1-3.3.6, Instituto Superior Técnico, Lisbon, Portugal.
- [3] Dahm, W.J.A. (1992) Experimental studies of the fine scale structure of mixing in turbulent flows. Invited Paper, Proceedings of the Thirteenth Symposium on Turbulence, University of Missouri-Rolla, Rolla, MO.
- [4] Nishino, N. Kasagi & Hirata, M. (1989) Three-dimensional particle tracking velocimetry based on automated digital image processing; *J. Fluids Eng.* 111, 384.
- [5] Papantoniou, D. & Maas, H.-G. (1990) Recent advances in 3-D particle tracking velocimetry; in *Proceedings of the 5th Symposium on Applications of Laser Techniques to Fluid Mechanics* (Instituto Superior Técnico, Lisbon).
- [6] Haussmann, G. & Lauterborn, W. (1980) Determination of size and position of fast moving gas bubbles in liquids by digital 3-D image processing of hologram reconstructions; *Appl. Opt.* 19, 3529.
- [7] Malyak, P.H. & Thompson, B.J. (1984) Particle displacement and velocity measurement using holography; *Opt. Eng.* 23, 567.
- [8] Scherer, J. & Bernal, L.P. (1988) Resolution characteristics of holographic particle image velocimetry; AIAA Paper No. 92-0009, AIAA, Washington, D.C.
- [9] Dahm, W.J.A. & Buch, K.A. (1990) High-resolution three-dimensional spatiotemporal measurements of the conserved scalar field in turbulent shear flows; in *Turbulent Shear Flows* (Springer-Verlag, Berlin).
- [10] Dahm, W.J.A., Southerland, K.B. & Buch, K.A. (1991) Four-dimensional laser induced fluorescence measurements of conserved scalar mixing in turbulent flows; in *Applications of Laser Techniques to Fluid Mechanics* (Springer-Verlag, Berlin).
- [11] Dahm, W.J.A., Southerland, K.B. & Buch, K.A. (1991) Direct, high-resolution, four-dimensional measurements of the fine scale structure of  $Sc \gg 1$  molecular mixing in turbulent flows; *Phys. Fluids A* 3, 1115.
- [12] Truesdell, C., *The Kinematics of Vorticity*, Indiana Univ. Press, 1954.

- [13] Balint, J.-L., Wallace, J.M. & Vukoslavcevic, P. (1991) The velocity and vorticity vector fields of a turbulent boundary layer. Part 2. Statistical properties. *J. Fluid Mech.* **228**, 53-86.
- [14] Vukoslavcevic, P., Wallace, J.M. & Balint, J.-L. (1991) The velocity and vorticity vector fields of a turbulent boundary layer. Part 1. Simultaneous measurement by hot-wire anemometry. *J. Fluid Mech.* **228**, 25-51.
- [15] Corrsin, S. & Kistler, A.L. (1954) The free-stream boundaries of turbulent flows. NACA TN 3133.
- [16] Foss, J.F. (1981) Advanced techniques for transverse vorticity measurements. In *Proc. 7th Symp. on Turbulence*, University of Missouri-Rolla, Rolla, MO, 208-218.
- [17] Foss, J.F., Ali, S.K. & Haw, R.C. (1987) A critical analysis of transverse vorticity measurements in a large plane shear layer. In *Advances in Turbulence* (eds. G. Comte-Bellot & J. Mathieu), 446-455, Springer, Berlin.
- [18] Foss, J.F., Klewicki, C.L. & Disimile, P.J. (1986) Transverse vorticity measurements using an array of four hot-wires. NASA CR 178098.
- [19] Foss, J.F., & Wallace, J.M. (1989) The measurement of vorticity in transitional and fully-developed turbulent flows. In *Advances in Fluid Mechanics* (ed. M. Gad-el-Hak), Lecture Notes in Engineering **45**, 263-321, Springer, Berlin.
- [20] Haw, R.C., Foss, J.K. & Foss, J.F. (1989) The vortical properties of the high speed region in a plane shear layer and its parent boundary layer. In *Advances in Turbulence* (eds. H.-H. Fernholz & H.E. Fielder), 90-95, Springer, Berlin.
- [21] Kastrinakis, E.G., Eckelmann, H. & Willmarth, W.W. (1979) Influence of the flow velocity on a Kovasznay-type vorticity probe. *Rev. Sci. Instruments* **50**, 759-767.
- [22] Kastrinakis, E.G., Wallace, J.M., Willmarth, W.W., Ghorashi, B. & Brodkey, R.S. (1977) On the mechanism of bounded turbulent shear flows. In *Structure and Mechanisms of Turbulence I*. Lecture Notes in Physics **75**, 175-189.
- [23] Kastrinakis, E.G. & Eckelmann, H. (1983) Measurements of streamwise vorticity fluctuations in a turbulent channel flow. *J. Fluid Mech.* **137**, 165-186.
- [24] Kovasznay, L.S.G. (1954) Turbulence measurements. In *Physical Measurements in Gas Dynamics and Combustion*, Vol. 10. (eds. R.W. Landenburg, B. Lewis, R.N. Pease & H.S. Taylor), Princeton University Press.
- [25] Lang, D.B. (1985) Laser Doppler velocity and vorticity measurements in turbulent shear layers. Ph.D. Dissertation, Caltech, Pasadena.
- [26] Kit, E., Tsinober, A., Balint, J.L., Wallace, J.M., & Levich, E. (1987) An experimental study of helicity related properties of a turbulent flow past a grid.

*Phys. Fluids* **30**, 3323-3325.

- [27] Kit, E., Tsinober, A., Tejtcl, M., Balint, J.L., Wallace, J.M., & Levich, E. (1988) Vorticity measurements in turbulent grid flows. *Fluid Dyn. Res.* **3**, 289-294.
- [28] Tsinober, A., Kit, E., & Dracos, T. (1992) Experimental investigation of the field of velocity gradients in turbulent flows. *J. Fluid Mech.* **242**, 169-192.
- [29] Wallace, J.M. (1986) Methods of measuring vorticity in turbulent flows. *Expts. in Fluids* **4**, 61-71.
- [30] Willmarth, W.W. & Bogar, T.J. (1977) Survey and new measurements of turbulent structure near the wall. *Phys. Fluids* **20**, S9-S21.
- [31] Willmarth, W.W. & Lu, S.S. (1972) Structure of the Reynolds stress near the wall. *J. Fluid Mech.* **55**, 65-92.
- [32] Adrian, R.J. (1991) Particle-imaging techniques for experimental fluid mechanics. *Ann. Rev. Fluid Mech.* **23**, 261-304.
- [33] Adrian, R.J. (1986) Multi-point optical measurements of simultaneous vectors in unsteady flow - a review. *Int. J. Heat & Fluid Flow* **7**, 127-145.
- [34] Lauterborn, W. & Vogel, A. (1984) Modern optical techniques in fluid mechanics. *Ann. Rev. Fluid Mech.* **12**, 223-244.
- [35] Gad-el-Hak, M. (1989) Advances in Fluid Mechanics Measurements, Springer, Berlin.